2020 ROBARTS RESEARCH RETREAT

Robarts Association of Trainees

FRIDAY, JUNE 19TH 10AM-5PM

Register @ https://tinyurl.com/yd8wsxa5

ONLINE VIA **ZOOM**

PRESENTED BY THE ROBARTS ASSOCIATION OF TRAINEES

WELCOMING ADDRESS
ROBARTS RESEARCH RETREAT

Dear Attendees,

Welcome to the **7th annual Robarts Retreat Retreat**! This year marks our first time holding this Robarts tradition virtually. Despite a new format, we hope that the Retreat will still serve to bring our community together and incite meaningful discussion on relevant issues. With normal life and research beginning to resume, this is a great time to look back on the lessons we have learned from this pandemic. We are excited to hear from our keynote speaker, Dr. Eric Arts, on the contributions Western has made to the global effort in developing effective measures against the virus. Furthermore, we look forward to a discussion on the impacts of this pandemic from an esteemed panel of Western researchers, Dr. Saverio Stranges, Dr. Prachi Srivastava, and Dr. Jacob Shelley. This year's Retreat features over 50 talks from trainees, and we are excited for you all to witness the cutting-edge research being done at the institute.

We are supported by many individuals who are integral to making this event possible. We would first like to thank Dr. Greg Dekaban, founder of the Retreat, and Dr. David Litchfield for his support of this event. We would like to extend a special thanks to Kristina Fornelos for her assistance and hard work supporting the council over the years. We would like to thank our Robarts Mentorship Committee, Dr. Arthur Brown, Dr. Maria Drangova, Dr. Andrew Pruszynski and Dr. Don Welsh for their insight and guidance. We would also like to acknowledge the individuals who have volunteered as judges during this Retreat. Last but not least, we would like to sincerely thank all members of the Robarts community for your continued commitment to our annual Robarts Research Retreat; without your presence, a successful Retreat would be impossible.

We are excited to share this day with you and hope you enjoy the event!

Sincerely,
2019-2020 Robarts Association of Trainees

(1) ***TianDuo Wang***, PhD candidate, Medical Biophysics (2) ***Ben Corrigan***, PhD student, Neuroscience
(3) ***Megan Roussy***, PhD student, Neuroscience (4) ***Nathan Orlando***, PhD student, Medical Biophysics
(5) ***Dimuthu Hemachandra***, PhD student, Biomedical Engineering (6) ***Kartik Pradeepan***, PhD candidate, Neuroscience
(7) ***Xin Yue Wang***, MSc Candidate, Medical Biophysics (8) ***Olivia Ghosh-Swaby***, PhD Candidate, Neuroscience

SUMMARIZED PROGRAM

ROBARTS RESEARCH RETREAT

OPENING ADDRESS - DR. DAVID LITCHFIELD — *10:00am-10:15am*
ZOOM ROOM A

KEYNOTE - DR. ERIC ARTS — *10:15am-11:00am*
ZOOM ROOM A - Insight into COVID-19 research at Western University

SHORT BREAK *11:00am-11:15am*

1. ORAL PRESENTATIONS — *11:15am-12:15pm*
ZOOM ROOM A & ZOOM ROOM B

LUNCH BREAK *12:15pm-12:45pm*

PANEL - DR. STRANGES | DR. SRIVASTAVA | DR. SHELLEY — *12:45pm-1:45pm*
ZOOM ROOM A - The Impact of COVID-19

SHORT BREAK *1:45pm-2:00pm*

2. ORAL PRESENTATIONS — *2:00pm-3:00pm*
ZOOM ROOM A & ZOOM ROOM B

3 MINUTE TALKS — *3:00pm-3:45pm*
ZOOM ROOM A & ZOOM ROOM B

SOCIAL HOUR — *3:45pm-4:30pm*
ZOOM ROOM C - I

CLOSING REMARKS - RATS — *4:30pm-4:45pm*
ZOOM ROOM A

Robarts Association of Trainees

FRIDAY, JUNE 19TH 10AM-5PM

Register @ https://tinyurl.com/yd8wsxa5

ONLINE VIA **ZOOM**

PRESENTED BY THE ROBARTS ASSOCIATION OF TRAINEES

STAY CONNECTED

ROBARTS RESEARCH RETREAT

JOIN THE RRR2020 SLACK
https://robartsretreat2020.slack.com

USE THE HASHTAG
#RRR2020

ROOM A
MEETING ID
931 6785 6084
PW: Register for password

zoom

ROOM B
MEETING ID
929 0480 8834
PW: Register for password

@robartsrats

Robarts Research Institute

www.robartsrats.com

Robarts Association of Trainees

FRIDAY, JUNE 19TH 10AM-5PM

Register @ https://tinyurl.com/yd8wsxa5

PRESENTED BY THE ROBARTS ASSOCIATION OF TRAINEES

TABLE OF CONTENTS
ROBARTS RESEARCH RETREAT

ROOM A

MEETING ID

931 6785 6084

PW: Register for password

ROOM B

MEETING ID

929 0480 8834

PW: Register for password

2020 ROBARTS RESEARCH RETREAT
GUEST SPEAKERS

KEYNOTE

10:15am - 11:00am

INSIGHT INTO COVID-19 RESEARCH AT WESTERN UNIVERSITY

DR. ERIC ARTS, PHD

Professor and Chair Department of Microbiology & Immunology, at the Schulich School of Medicine & Dentistry; Canada Research Chair in HIV Pathogenesis and Viral Control.

Dr. Arts is an internationally renowned scholar with career accomplishments encompassing more than 130 publications and book chapters as well as several patents and licensing agreements with industry. His main area of research is in HIV-1 pathogenesis, evolution, drug resistance, and molecular biology. The Arts lab has developed collaborations around the world, including in Zimbabwe, Cameroon, China, Belgium, UK, France, Brazil, and Argentina. Dr. Arts leads a multidisciplinary team of Schulich scientists at Western in the efforts towards establishing and testing an effective vaccine for SARS-CoV2, the virus causing COVID-19. At the same time, the team is also developing a 'vaccine bank' that would contain ready-made vaccines to be used rapidly at the start of another coronavirus outbreak.

PANEL

12:45pm - 1:45pm

THE IMPACTS OF COVID-19

DR. SAVERIO STRANGES, MD, PHD, FAHA

Professor and Chair of the Department of Epidemiology and Biostatistics at Western

Dr. Stranges is a public health physician and epidemiologist, whose expertise lies in chronic disease, global health and interdisciplinary research, being involved in several epidemiological studies and clinical trials both in high-income and low-income countries. Specifically, Dr. Stranges's research focuses on the epidemiology and prevention of chronic disease and aging, specifically regarding the role of lifestyles, environmental and psychosocial factors, such as dietary patterns, sleep behaviors social and geographical determinants of health. He is also interested in global health, especially in the area of cardio-metabolic disease in low-resource settings, as well as in interdisciplinary research.

DR. PRACHI SRIVASTAVA, PHD

Associate Professor in the Education and International Development at Western Member, World Bank Expert Advisory Council on Citizen Engagement

Prof. Srivastava's research is in global education policy and the right to education. Since the pandemic, she has been active in global public engagement and analysis on the effect of COVID-19 on the global education emergency which has caused the largest mass disruption of education in history. Prof. Srivastava is leading a high-level policy brief for the T20 Task Force, COVID-19 Multidisciplinary Approaches to Complex Problems, which will feed into the G20 Summit. She is also active on social media and in media engagement on the pandemic effects on education (CBC Radio-Canada, Globe & Mail, Reddit AMA, TVO).

DR. JACOB SHELLEY, SJD, LLB, LLM, MTS

Assistant Professor in the Faculty of Law and School of Health Studies

Prof. Shelley's primary area of interest and teaching is healthcare law and policy, and public law and policy, particularly in studying proper limits and role of law in promoting public health and preventing chronic disease. In addition, he is generally interested in issues that arise at the interface of law, healthy science, and ethics. Prof. Shelley's work has contributed to shaping policies at the federal levels, including at Health Canada and the Senate.

2020 ROBARTS RESEARCH RETREAT
FULL PROGRAM

MORNING

OPENING ADDRESS - DR. DAVID LITCHFIELD
10:00am-10:15am

ZOOM ROOM A

KEYNOTE - DR. ERIC ARTS
10:15am-11:00am

ZOOM ROOM A - Insight into COVID Research at Western University

This March, Western received a nearly one million dollar investment from the CIHR to join the global effort in curbing the spread of the COVID-19. This session is meant to provide an overview of the research currently being done at Western towards development of an effective vaccine for COVID-19 and provide insight into the exciting discoveries and challenges associated with this effort.

SHORT BREAK

1. ORAL PRESENTATIONS
11:15am-12:15pm

ZOOM ROOM A

NAME: ***Shirley Liu***
TITLE: Modeling and Characterizing Synchronous Bilateral Breast Cancer Metastasis in Mice Using Dual-Bioluminescence Imaging
SUPERVISOR: Dr. John Ronald

NAME: ***Liliana German-Castelan***
TITLE: Sexual dimorphism in Vesicular acetylcholine transporter (VAChT) regulation of plaque pathology in Alzheimer's disease knock-in mouse models
SUPERVISOR: Dr. Marco Prado, Dr. Vania Prado

NAME: ***Sam Papernick***
TITLE: Validation of 3D ultrasound segmentation reliability for quantifying trochlear knee cartilage degradation
SUPERVISOR: Dr. Aaron Fenster, Dr. Tom Appleton

NAME: ***Allison Diliott***
TITLE: White matter hyperintensity burden in PD patients harbouring rare NOTCH3 genetic variation
SUPERVISOR: Dr. Rob Hegele

NAME: ***Hareem Nisar***
TITLE: Tracking, Calibration and Characterization of a Single-element Ultrasound
SUPERVISOR: Dr. Terry Peters

NAME: ***Miriam Hewlett***
TITLE: Motion Correction in MRI using a Generative Adversarial Network: An Evaluation with the FastMRI Dataset
SUPERVISOR: Dr. Maria Drangova

ZOOM ROOM B

NAME: ***Vasiliki Tellios*** *11:15AM*
TITLE: Cannabinoid-1 receptor dysregulation during cerebellar development in nNOS-/- mice
SUPERVISOR: Dr. Wei-Yang Lu

NAME: ***Reid Vassallo*** *11:25AM*
TITLE: Deriving blood flow directions from neurosurgical videos using deep learning and dynamic linear models
SUPERVISOR: Dr. Terry Peters

NAME: ***Adrianna Tsang*** *11:35AM*
TITLE: Investigating the role of lysosomal exocytosis in Alzheimer's disease
SUPERVISOR: Dr. Stephen Pasternak

NAME: ***Maksym Sharma*** *11:45AM*
TITLE: Machine Learning with Texture Analysis Reveals Subclinical Emphysema In Thoracic X-ray Computed Tomography
SUPERVISOR: Dr. Grace Parraga

NAME: ***Naila Rahman*** *11:55AM*
TITLE: Validation of Advanced Approaches for Microstructural Diffusion MRI
SUPERVISOR: Dr. Corey Baron

NAME: ***Veronica Dubois*** *12:05PM*
TITLE: Development of molecular imaging technologies for monitoring the fate of T cell immunotherapies
SUPERVISOR: Dr. John Ronald, Dr. Paula Foster

FULL ABSTRACTS PG. 6-11

AFTERNOON

LUNCH BREAK *12:15pm-12:45pm*

PANEL - DR. STRANGES | DR. SRIVASTAVA | DR. SHELLEY *12:15pm-1:45pm*

ZOOM ROOM A - Impacts of COVID-19

A discussion on the many short and long-term impacts of the global COVID-19 pandemic on society. World renowned scientists at Western will provide unique perspectives on the epidemiology of the virus, ethical and law considerations, and social and educational impacts of this pandemic.

SHORT BREAK

2. ORAL PRESENTATIONS *2:00pm-3:00pm*

ZOOM ROOM A

NAME: ***Dana Broberg***
TITLE: Brain glutamate measurement in a triple transgenic model of Alzheimer's Disease
SUPERVISOR: Dr. Robert Bartha

NAME: ***Claire Park***
TITLE: An intrinsic registration method for ultrasound-guided breast lesion targeting under high-resolution positron emission mammography localization
SUPERVISOR: Dr. Aaron Fenster

NAME: ***Alycia Crooks***
TITLE: Understanding muscarinic-mediated signaling in astrocytes using DREADDs for the control of neuroinflammation and cognition
SUPERVISOR: Drs. Vania Prado, Dr. Marco Prado, Dr. Tim Bussey

NAME: ***Sydney Wilson***
TITLE: Parametric design of focussed collimator for real-time intra-operative gamma detection
SUPERVISOR: Dr. David Holdsworth

NAME: ***Kate Onuska***
TITLE: In vivo molecular imaging of the cholinergic projection system in mice
SUPERVISOR: Dr. Taylor Schmitz, Dr. Marco Prado

NAME: ***Jessica Rodgers***
TITLE: Intraoperative visualization of intracavitary gynecologic brachytherapy applicators using 3D transrectal ultrasound
SUPERVISOR: Dr. Aaron Fenster

ZOOM ROOM B

NAME: ***Emily Qin*** *2:00PM*
TITLE: Investigating stroke origin from thrombus cellular composition
SUPERVISOR: Dr. Maria Drangova; Dr. Spencer Christiansen

NAME: ***Alicia Cronin*** *2:10PM*
TITLE: Spinal cord compression severity leads to cortical reorganization in patients with cervical spondylotic myelopathy
SUPERVISOR: Dr. Robert Bartha

NAME: ***Leah Groves*** *2:20PM*
TITLE: Evaluation of a mixed-reality first person point of view needle navigation system
SUPERVISOR: Dr. Terry Peters, Dr. Elvis Chen

NAME: ***Spencer Arbuckle*** *2:30PM*
TITLE: Integration of tactile information from multiple fingers in human primary sensory cortex measured using high-resolution fMRI
SUPERVISOR: Dr. Joern Diedrichsen, Dr. Andrew Pruszynski

NAME: ***Olivia Sehl*** *2:40PM*
TITLE: Using fluorine-19 MRI cell tracking to detect and quantify peripheral blood mononuclear cells and regulatory T cells in vivo
SUPERVISOR: Dr. Paula Foster

NAME: ***Ornela Kljakic*** *2:50PM*
TITLE: Motivation and cue-directed effort are regulated by acetylcholine/glutamate co-transmission from striatal cholinergic interneurons
SUPERVISOR: Dr. Marco Prado, Dr. Vania Prado

FULL ABSTRACTS PG. 12-17

AFTERNOON (CONTINUED)

3 MINUTE TALKS

3:00pm-3:45pm

ZOOM ROOM A

NAME: ***Julieta Lazarte*** (Dr. Hegele)
TITLE: "Lone" Atrial Fibrillation is Primarily Polygenic

NAME: ***Julia Gevaert*** (Dr. Paula Foster)
TITLE: Development of Iron Oxide Nanoparticles for Magnetic Particle Imaging

NAME: ***Hayley Shanks*** (Dr. Taylor W. Schmitz)
TITLE: Plasma phosphatidylcholines are associated with the longitudinal grey-matter integrity of the basal forebrain

NAME: ***Gabriel Mattatall*** (Dr. Ravi S Menon)
TITLE: Automatic determination of the regularization weighting for wavelet-based compressed sensing MRI reconstructions

NAME: ***Leen (Yutong) Wu*** (Dr. Jenn Biltcliffe, Dr. David E. Carter)
TITLE: Single Cell RNA Sequencing

NAME: ***Joseph Umoh***
TITLE: Micro-computed Tomography Determination of the Relationship Between Visceral Adipose Tissue and Whole-Body Adipose Tissue in Rats and Mice

NAME: ***Spencer Cristiansen*** (Dr. Maria Drangova)
TITLE: Deep learning prediction of stroke thrombus RBC content from multiparametric MRI ex vivo

NAME: ***Natasha Knier*** (Dr. Paula Foster)
TITLE: Monitoring a patient derived xenograft model of breast cancer with magnetic particle imaging and bioluminescence imaging

NAME: ***Nafis Hossain*** (Dr. Ali R. Khan, Dr. Teneille Gofton)
TITLE: Determining the relationship between early and rapid brain atrophy on clinical outcomes in refractory status epilepticus: a retrospective analysis

NAME: ***Sawyer Badiuk*** (Dr. Eugene Wong, Dr. Jeff Chen)
TITLE: Prevention of new and recurrent breast cancer brain metastases using immune response-guided radiation therapy

NAME: ***Nourhan Shalaby*** (Dr.John Ronald, Dr. Timothy Scholl)
TITLE: A PET/MRI Reporter Gene Cell System for cell tracking

NAME: ***Jordan Krupa*** (Dr. Stephen Pasternak)
TITLE: Examining the regulation of the macropinocytosis of Amyloid Precursor Protein

ZOOM ROOM B

NAME: ***Tasnim Reza*** (Dr. Michael B. Boffa)
TITLE: Anti-metastatic role of Thrombin activatable fibrinolysis inhibitor (TAFI) and thrombomodulin in the breast cancer microenvironment

NAME: ***Amer Youssef*** (Dr. Marlys Koschinsky)
TITLE: Direct Evidence for the Intracellular Non-Covalent Interaction of Apolipoprotein(a) and ApolipoproteinB100 during Lipoprotein(a) Biosynthesis

NAME: ***Farah Mushtaha*** (Dr. Corey Baron, Dr. Ali Khan)
TITLE: Microstructural characterization and Visualization a 3D printed phantom using diffusion MRI and microscopy

NAME: ***Patrick Carnahan*** (Dr. Terry Peters, Dr. Elvis Chen)
TITLE: Multi-view 3D echocardiography volume compounding for mitral valve procedure planning

NAME: ***Mahsa Bataghva*** (Dr. James C. Lacefield)
TITLE: Ultrasound-Based Microvascular Parameters for Classification of Anti-Angiogenic Tumor Treatment Response: A Scalable Preclinical Approach

NAME: ***Kierstin Melo*** (Dr. Paula Foster)
TITLE: Comparing detection limits of Magnetic Particle Imaging (MPI) to Magnetic Resonance Imaging (MRI) using super paramagnetic iron oxide nanoparticles in a breast cancer metastasis model

NAME: ***Crystal McLellan***
TITLE: MiRNA expression in motor neurons of the oculomotor nucleus in ALS

NAME: ***Neil Donison*** (Dr. Michael Strong, Dr. Arthur Brown)
TITLE: Characterization of an N-terminal tau cleavage fragment associated with the phosphorylation of tau at Thr175

NAME: ***Jake Valsamis*** (Dr. Corey Baron)
TITLE: Robust Retrospective Eddy Current Correction for Diffusion MRI

NAME: ***Madeline Gilchrist*** (Dr. Penny MacDonald, Dr. Brian Corneil)
TITLE: Dopaminergic modulation of a fast visuomotor pathway in Parkinson's disease

NAME: ***William Anderson*** (Dr. David Holdsworth)
TITLE: Design and 3D Printing of Wireless Load Cells for Biomedical Applications

FULL ABSTRACTS PG. 18-28

AFTERNOON (CONTINUED)

SOCIAL HOUR - (HOSTED BY RATS COUNCIL)

3:45pm-4:30pm

ACTIVITY/TOPIC: Robarts Recipes
HOSTED BY: Ben Corrigan
ZOOM ROOM C
MEETING ID: 916 5344 0263

ACTIVITY/TOPIC: Full Body HIITness (30 minute workout and cool down)
HOSTED BY: Olivia Ghosh-Swaby - **wear workout attire**
ZOOM ROOM D
MEETING ID: 970 9733 6936

ACTIVITY/TOPIC: Graduate School and Professional Development
HOSTED BY: Megan Roussy
ZOOM ROOM E
MEETING ID: 813 7024 9518

ACTIVITY/TOPIC: Artificial Intelligence @ Robarts
HOSTED BY: Nathan Orlando and Dimuthu Hemachandra
ZOOM ROOM F
MEETING ID: 949 5608 3489

ACTIVITY/TOPIC: Hobbie Hour
HOSTED BY: Xin Yue Wang
ZOOM ROOM G
MEETING ID: 965 5143 1108

ACTIVITY/TOPIC: News in Neuroscience
HOSTED BY: Kartik Pardeepan
ZOOM ROOM H
MEETING ID: 968 318 3446

ACTIVITY/TOPIC: Robarts Watchparty
HOSTED BY: TianDuo Wang
ZOOM ROOM I
MEETING ID: 986 0701 9000

Register for password

CLOSING REMARKS - RATS

4:30pm-4:45pm

ZOOM ROOM A

1. ORAL PRESENTATIONS (ROOM A)

11:30am - 12:30pm

Modelling and Characterizing Synchronous Bilateral Breast Cancer Metastasis in Mice Using Dual-Bioluminescence Imaging

Shirley Liu, Nivin N Nyström, John J Kelly, Amanda M Hamilton, Yanghao Fu, John A Ronald

Synchronous bilateral breast cancer (SBBC) is the development of malignant lesions in both breasts within 12 months. It occurs in approximately 2% of breast cancer patients, and compared to women with unilateral breast cancer, SSBC patients have higher rates of metastasis and lower overall survival. However, little is known about the metastatic properties of cells from each tumour, which can directly contribute to patient outcome. Here we developed the first mouse model of SBBC by orthotopically implanting human breast cancer cells into bilateral mammary fat pads, and used non-invasive imaging to study the biodistribution of spontaneously metastasizing cells from each tumour. To track cells from each tumor, we engineered them to express two recently developed and highly sensitive BLI reporters called Akaluc or Antares2 and performed dual-bioluminescence imaging (dual-BLI) for 6 weeks after implantation (n=10 mice). Cells were also co-engineered with either the fluorescence reporter tdTomato or zsGreen for endpoint fluorescence microscopy. Dual-BLI showed lung metastasis from both primary tumors in nine of 10 mice as early as day 21 (Fig. 1A), and BLI signal from metastases continued to increase over time (Fig. 1 B). Unexpectedly, microscopy revealed that the majority of metastases (60%) were composed of a mixture of both tdTomato and zsGreen cells from both primary tumors. Our SBBC model suggests metastatic cross-seeding is a common occurrence, which may contribute to tumour heterogeneity and treatment resistance. These unexpected findings may explain the worse outcome of SBBC patients and should provide future insight on patient treatment and management.

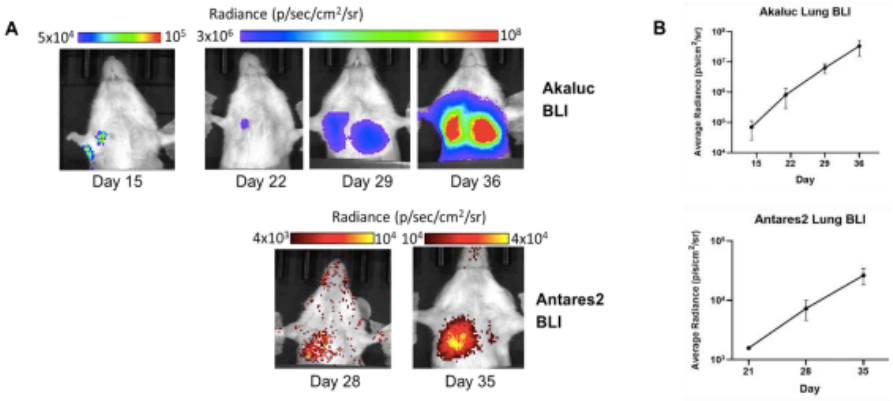

Figure 1. Dual-BLI of lung metastases of contralateral Akaluc- and Antares2-expressing mammary fat pad tumors. A) Representative images of Akaluc BLI and Antares2 BLI of lung metastasis. B) Quantification of Akaluc and Antares2 lung BLI over time (n=10).

Sexual dimorphism in Vesicular acetylcholine transporter (VAChT) regulation of plaque pathology in Alzheimer's disease knock-in mouse models

Liliana German-Castelan, Takashi Saito, Takaomi C Saido, Marco A. M. Prado1,2,5,6, Vania F. Prado

Cholinergic deficiency is a characteristic of many neurodegenerative disorders including Alzheimer's disease (AD). Decreased levels of the vesicular acetylcholine transporter (VAChT) have been detected in AD patients and imaging data suggests that VAChT levels can predict human pathology, however, whether changes in VAChT are associated with plaque aggregation is unknown. To test for a causal relationship between VAChT levels and A plaques, we crossed a humanized APP knock-in (KI) mouse, carrying 2 AD-associated mutations, with mice lacking VAChT in forebrain neurons. We quantified the area covered by plaques in the cortex and the levels of insoluble A in 9 and 12-month-old males and females. We found that elimination of VAChT increased plaque area and A levels. Remarkably, these changes were seen only in males, while females remained unaffected. Also, to study whether increased VAChT regulates pathology, we crossed APPKI mice carrying 3 AD mutations with mice overexpressing VAChT. We analyzed plaque pathology in males and females at 2, 3 and 6 months of age and we found a decrease in plaque area and A levels in 2 and 3-month-old VAChT-overexpressing males; females were not affected. Interestingly, at 6 months VAChT regulation of plaque pathology is lost, suggesting that VAChT influences early stages of A deposition in these mice. These results indicate a causal relationship between VAChT and plaque pathology in a humanized AD mouse model and point to a sexually dimorphic response in mice due to changes in VAChT, a topic that should be explored in humans in the future.

Validation of 3D ultrasound segmentation reliability for quantifying trochlear knee cartilage degradation

Sam Papernick, R Dima, D Gillies, T Appleton, A Fenster

Introduction: Knee Osteoarthritis (KOA) is one of the most prevalent chronic health conditions in Canada and can lead to cartilage degradation, mobility limitations, and severe pain. There is a great clinical need for an objective imaging-based point-of-care tool to assess KOA status, progression, and response to treatment. We aim to validate a handheld 3D ultrasound (US) device we developed for quantifying femoral articular cartilage (FAC) volumes in healthy subjects against the current standard of MRI. Methods: Knee images of 25 healthy volunteers were acquired with 3D US and accompanying 3.0T MRI. The FAC was segmented by 2 raters with repeated segmentations conducted on 5 cases. 3D US and MRI segmentations were registered using a semi-automated surface-based registration algorithm, and MRI segmentations were trimmed to match the FAC region segmented from 3D US. Intra-rater (n = 5) and inter-rater (n = 25) reliabilities were assessed using intraclass correlation coefficients (ICCs) calculated from segmentation volumes, and a Spearman correlation was conducted between MRI and 3D US volumes. Results: 3D US intra-rater ICC were 0.99 for both raters while inter-rater ICC was 0.95. MRI intra-rater ICC were 0.97 and 0.90 for each rater while inter-rater ICC was 0.83. Spearman correlation revealed $\rho = 0.88$ ($p < 0.0001$, $n = 25$). Significance: 3D US can be used to quantify healthy trochlear FAC volumes with higher reliability than MRI. Our 3D US device has the potential to increase the quality-of-life of KOA patients by reducing the need for MRI in clinical trials and future care.

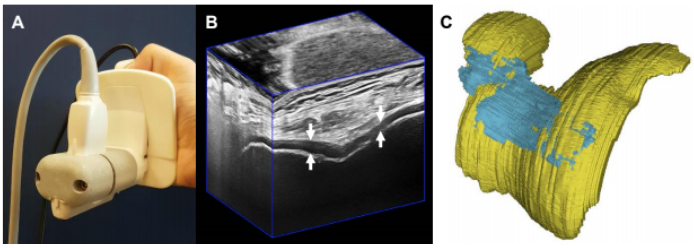

Figure 1. (A) Image of our handheld 3D US acquisition device in the hand of a user. A custom 3D-printed mount that matched the shape of the transducer was used to securely attach the conventional US transducer to our device. (B) 3D US image of healthy trochlear FAC indicated by the anechoic region outlined by the white arrows. 3D US images can be manipulated in 3D space and can be sliced at any arbitrary plane to provide additional perspectives. (C) Overlaid segmentations of the FAC following registration of MRI (yellow) and 3D US (blue).

White matter hyperintensity burden in PD patients harbouring rare NOTCH3 genetic variation

Allison A. Dilliott, Joel Ramirez, Malcolm A. Binns, David P. Breen, Emily C. Evans, Derek Beaton, Paula M. McLaughlin, Donna Kwan, Melissa F. Holmes, Miracle Ozzoude, Christopher J.M. Scott, Stephen C. Strother, Sean Symons, Richard H. Swartz, David Grimes, Mandar Jog, Mario Masellis, Sandra E. Black, Anne Joute, Connie Marras, Ekaterina Rogaeva, Robert A. Hegele, Anthony E. Lang, on behalf of ONDRI Investigators

Cerebral autosomal dominant arteriopathy with subcortical infarcts and leukoencephalopathy (CADASIL) is caused by heterozygous pathogenic mutations in the Notch Receptor 3 gene (NOTCH3). Patients present with ischemic strokes, cognitive impairment, and white matter hyperintensities (WMH); however, rare cases present with late-onset parkinsonism. We aimed to investigate the association between NOTCH3 variants and WMH in Parkinson's disease (PD) patients. We used a next-generation sequencing gene panel to sequence 139 PD patients and identified 13 (~9%) harbouring rare, non-synonymous NOTCH3 variants. Patients were also imaged using magnetic resonance imaging (MRI; 3T) and underwent robust clinical characterization. Using a Bayesian linear model, we observed a doubling of WMH volume between the NOTCH3 variant negative patients and the NOTCH3 variant positive patients, with a multiplicative effect of ~2.2 (between 1.2 and 3.7, 95% probability), accounting for conventional vascular risk factors. Interestingly, no differences in cognition or motor phenotypes were identified between the groups; however, suggested relationships were observed between WMH volumes and cognition (r=-0.19, C.I: -0.32, -0.02) and motor phenotypes (r=0.14, C.I.: -0.03, 0.30), across all PD patients. This is the first report suggesting that rare, non-synonymous NOTCH3 variants may have a role in WMH burden in cases of idiopathic PD. Although cognition and motor phenotypes were not different between NOTCH3 variant positive and negative patients, this may have resulted from limited sample size. It is recommended that future studies examining WMH volumes in PD are complimented with genomic analysis for NOTCH3 variation.

Tracking, Calibration and Characterization of a Single-element Ultrasound

Hareem Nisar, John Moore, Elvis Chen, and Terry Peters

Introduction: This work aims at developing a simple, anatomically and haptically realistic vascular phantom, compatible with intravascular and intracardiac ultrasound. The low-cost, dual-layered phantom bridges the gap between traditional wall-only and wall-less phantoms by showing both the vessel wall and surrounding tissue in ultrasound. This phantom can better assist testing of intravascular devices, blood flow studies and validation of algorithms for intravascular and intracardiac systems. Methods: Polyvinyl-alcohol cryogel and scattering agent were used to obtain vessel and tissue mimicking materials. Inferior vena cava and renal bifurcations were targeted and modelled in a CAD software. A mould and container were 3D printed for shaping the desired vessel wall. Three phantoms were prepared by varying the concentrations of scattering agent and the number of freeze-thaw cycles to which the phantom layers are subjected. Each phantom was evaluated using ultrasound imaging using the ForeightTM ICE probe. Geometrical validation was provided by comparing CAD design to a CT scan of the phantom. Results: Desired vascular phantom was achieved using 2.5% and 0.05% w/w scattering agent concentration in vessel and tissue mimicking layer, respectively. Imaging of the three phantoms showed that increasing the number of freeze-thaw cycles did not significantly enhance the image contrast. Comparison with CT reported an average error of 0.9 mm for the lumen diameter. Conclusion: The phantom is anatomically realistic when imaged with intracardiac ultrasound and provides a smooth lumen for the probe and catheter to maneuver. The simple construction technique also provides a workflow for designing complex, multi-layered arterial phantoms.

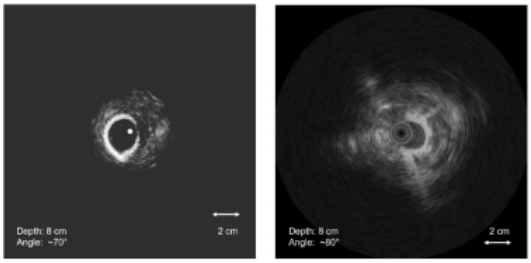

Figure 1: Conavi Foresight ICE imaging comparison between the phantom designed (left) and the animal IVC image (right) at a radial depth of 8 cm.

Motion Correction in MRI using a Generative Adversarial Network: An Evaluation with the FastMRI Dataset

Miriam Hewlett, Ivailo Petrov, and Maria Drangova

As many as 1 in 5 MRI exams require that at least one scan be repeated due to motion artifacts. Deep learning has the potential to provide a general solution for motion correction, requiring no pulse sequence modifications or additional hardware. Previous work by our group has successfully trained a conditional generative adversarial network (cGAN) to correct simulated motion artifacts in brain MRIs; however, the dataset examined in this case was limited to scans of healthy subjects acquired on a single scanner with the same contrast. The objective of this work was to modify our cGAN for motion correction on a more diverse dataset, with the hope that it will generalize well to more realistic clinical cases. The cGAN was trained, validated, and tested with motion artifacts simulated in the open source NYU fastMRI Dataset, which includes brain images with a variety of neurological pathologies and contrasts acquired using 11 scanners across 5 sites. These volumes were divided into training, validation, and testing sets (3754, 921, and 1167 volumes, respectively). Motion correction with the cGAN reduced the mean MAE from 0.076 ± 0.032 to 0.049 ± 0.018 (mean ± standard deviation) in the validation dataset. However, many images still showed residual motion artifacts or blurring. Next steps will focus on training the cGAN for motion correction with individual contrasts, making use of transfer learning. If successful, this motion correction technique would be relatively simple to apply in practice, as it requires no modifications to image acquisition or additional hardware.

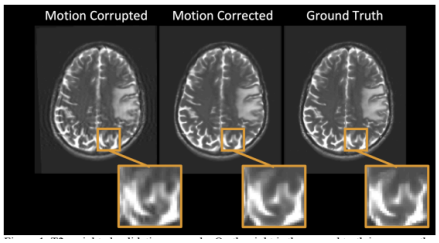

Figure 1. T2-weighted validation example. On the right is the ground truth image, on the left that same image with simulated motion corruption. The central image was obtained through motion correction with the cGAN network.

Cannabinoid-1 receptor dysregulation during cerebellar development in nNOS-/- mice

Vasiliki Tellios, Ravneet Nagra, Matthew Maksoud, Wei-Yang Lu

Cerebellar ataxia is a disease that can be inherited or can arise from a brain injury or chronic alcohol exposure, with symptoms such as difficulty walking and loss of fine movement control. Although movement therapies exist to help manage the symptoms, a definitive therapeutic treatment for cerebellar movement disorders has yet to emerge. Recently, cannabis has been thought of as a potential treatment to alleviate motor symptoms associated with ataxia, however the efficacy of cannabis use for movement disorders remains controversial. Nitric oxide (NO) is a neurotransmitter that is known to have implications in cerebellar ataxia and is also associated with the endocannabinoid pathway in the cerebellum. Therefore, this study aimed to determine whether NO levels in the cerebellum can affect this endocannabinoid pathway, particularly cannabinoid-1 receptors (CB1Rs), using a mouse model that lacks the ability to create nitric oxide (nNOS-/-). Using immunohistochemistry, western blotting, and organotypic slice cultures, we determined that nitric oxide is necessary to regulate CB1Rs and downstream proteins throughout cerebellar development. Specifically, nNOS-/- cerebella display less CB1Rs in adulthood compared to wildtype cerebella, and show elevated levels of diacylglycerol lipase-α, an enzyme that synthesizes endocannabinoids. As well, CB1R expression levels can be recovered in nNOS-/- ex vivo cerebellar slices with the addition of NO. Overall, these data suggest that low levels of NO in adulthood – characteristic of particular cerebellar ataxias – may result in lower levels of CB1Rs, potentially contributing to the ataxic phenotype associated with decreased NO synthesis.

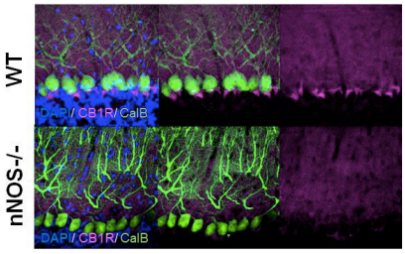

Figure 1. CB1R expression and localization is altered in nNOS-/- cerebella. CB1R expression is specifically localized to Purkinje neurons (green stain – CalB) both on the dendrites and axon hillock of the neuron. In nNOS-/- cerebella, significantly less CB1R staining (magenta) is seen, specifically within the dense axon hillock region. This finding may speak to the dysregulated output response of Purkinje neurons, leading to loss of motor coordination.

Deriving blood flow directions from neurosurgical videos using deep learning and dynamic linear models

R. Vassallo, A.J. McLeod, S.P. Lownie, H. Fukuda, H. Kasuya, B.W.Y. Lo, T. Peters, Y Xiao

Introduction: Neurovascular surgery involves the repair of diseased blood vessels associated with the brain and spine, including arteriovenous malformations (AVM) resection, aneurysm repair, and carotid endarterectomy (CEA). Surgical microscopes are routinely used across neurosurgery in general, providing convenient access to videos of surgical sites. In AVM surgery, it is crucial to correctly identify the direction of blood flow in vessels feeding and draining the diseased region. However, it is virtually impossible to differentiate these with visual inspection alone. Methods: For preliminary validation, 5-10 second videos were obtained retrospectively from 4 neurovascular surgeries. The operating surgeon in each case documented which direction the blood was flowing in specific vessels, creating the ground truths. These videos underwent deep-learning-based motion attenuation with a pre-trained model to mitigate physiological motions, and dynamic linear modelling (DLM) was used to find the periodic changes in the vessel and derive the direction of blood flow. Then, an arrow indicating the flow direction is automatically overlaid onto the video frame. Results: In all cases considered in this preliminary validation, the direction found in this preliminary validation matched the ground truth. Our results are shown in Fig. 1. Conclusions: Our preliminary results suggest that the proposed workflow can be used to identify the direction of flow in blood vessels during neurovascular surgery, but future studies with more rigorous validation are required. We also plan to make this technique more resilient in the face of specular highlights, as we currently cannot determine flow direction in the presence of these saturated pixels (Fig. 1(a)).

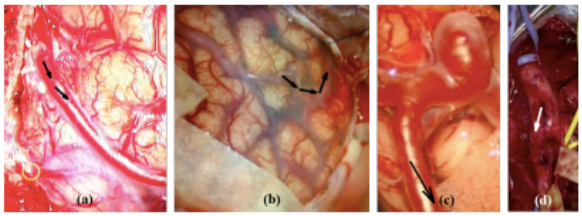

Figure 1. Annotated views of the correct blood flow directions found using our technique in retrospective analysis of: (a,b) AVM resection cases, (c) aneurysm repair, and (d) carotid endarterectomy (CEA)

Investigating the role of lysosomal exocytosis in Alzheimer's disease

Adrianna Tsang, Shany Lahan, Claudia Seah, Jordan Krupa, Stephen Pasternak1,2

Alzheimer's disease is driven by a balance of beta-amyloid (Aβ) production and clearance. This project aimed to investigate the cellular pathways contributing to abnormal trafficking of aggregated Aβ, with a specific focus on establishing the role of lysosomal exocytosis in neuronal models of AD. We hypothesized that lysosomal secretion is mediated by Rab27b in neurons and that dysregulation of lysosomal exocytosis leads to an intracellular build-up of Aβ (Figure 1). This study screened potential proteins implicated in lysosomal exocytosis (Rab27b, Munc13-4 and synaptotagmin-7). Experiments were performed in SN56 cells transfected to express our proteins of interest (wild-type, mutant and targeted siRNA), loaded with Aβ42, and treated with ionomycin to induce exocytosis. Images were acquired by confocal microscopy, while total internal reflection fluorescence (TIRF) microscopy was performed to capture videos of molecular events occurring within 250nm from the plasma membrane. Parallel experiments are being conducted in mouse cortical neurons, cortical neurons derived from hiPSCs and human cortical neurons cultured from epilepsy patients. In SN56 cells, we have captured lysosomes collapsing at the membrane by TIRF microscopy (Figure 2). Additionally, there is reduced Aβ and lysosomal colocalization after inducing exocytosis, indicating secretion of Aβ from lysosomes. Overexpression of Rab27b N133I mutant significantly increases lysosomal exocytosis of Aβ compared to wild-type, suggesting a role for Rab27b in this process. Our preliminary results provide more insight into the presence of regulated lysosomal exocytosis as a novel clearance pathway in neurons and could identify potential pharmacological targets that regulate clearance of toxic Aβ in AD.

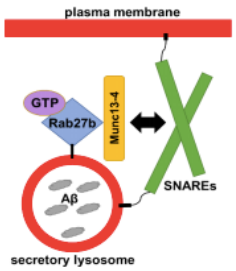

Figure 1: Proposed model of molecular machinery implicated in lysosomal exocytosis

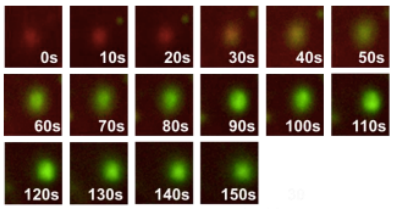

Figure 2: Lysosomes were marked by a pH-sensitive dual-fluorescent tag (pHluorin-LAMP1-mAppleFP) to observe timing and number of secretory events by TIRF microscopy. Change in colour indicates lysosome collapsing at plasma membrane after ionomycin treatment over 150 seconds

Machine Learning with Texture Analysis Reveals Subclinical Emphysema In Thoracic X-ray Computed Tomography

Maksym Sharma, Andrew Westcott, Jonathan L MacNeil, David G McCormack, and Grace Parraga

Purpose: To use machine-learning and texture analysis to uncover novel CT features that explain MRI apparent diffusion coefficients consistent with airspace enlargement or emphysema. METHODS: Ex-smokers without spirometry evidence of airflow limitation provided informed consent to an approved protocol and underwent spirometry, hyperpolarized gas MRI and thoracic CT. Participants were dichotomized based on diffusing capacity of the lungs for carbon-monoxide (DLCO) threshold of ≥75%. CT texture features were extracted from a novel 3-dimensional extension of gray-level run-length-matrices, gap-length-matrices, size-zone-matrices and co- occurrence-matrices. Principal component analysis and forward selection logistic-regression were used to select significantly contributing CT features. Single and ensemble-based machine-learning classifiers were compared. Model performance was evaluated using area-under-the-receiver-operator-characteristic-curve (AUC), sensitivity and specificity. Results: We evaluated 65 ex-smokers (Normal DLCO: n=41, Abnormal DLCO: n=24) without significant differences in pulmonary function tests and relative-area-of-the-lung <-950 Hounsfield Units (RA950) between groups. Long-run-emphasis and run-percentage were statistically different (p=0.001 and p=0.022) between groups and significantly but moderately correlated with MRI apparent diffusion coefficient measurements (r=0.48, p<0.001 and r=-0.46, p<0.001 respectively). Quadratic-SVM achieved the highest classification accuracy of 80%. Conclusions: Using machine-learning we identified CT texture features that differentiated ex-smokers with and without mild emphysema not revealed using conventional CT measurements such as RA950. In other words, machine-learning revealed that greater long-run-emphasis and diminished run-percentage reflect homogeneous CT textures that are related to mild parenchymal emphysematous disease. This is important because until now it has been impossible to measure mild airspace enlargement using only CT lung tissue attenuation values.

Figure 1: Demographics, pulmonary-function, best model and feature comparison results in ex-smoker subgroups.

Ex-smokers : (*n=65*)	DL_{CO}≥75%$_{pred}$ (*n=41*)	DL_{CO}<75%$_{pred}$ (*n=24*)	P-value
Age	67 (9)	71 (9)	0.18
Sex Female (%)	12 (29)	14 (58)	**0.02**
FEV_1 %$_{pred}$	103 (16)	94 (18)	0.05
DL_{CO}	91 (12)	56 (13)	**<0.001**
6MWD	438 (66)	363 (94)	**0.001**
RA_{950} %	1.2 (1.1)	1.1 (1.0)	0.7
ADC cm^2/s	0.26 (0.03)	0.30 (0.04)	**<0.001**
Feature 1 - LRE	42 (3)	48 (6)	**0.001**
Feature 2 - RP	0.345 (0.009)	0.333 (0.012)	**0.02**

Classifier	AUC	Sensitivity	Specificity	Accuracy
Quadratic SVM	0.77	85.7 %	76.5 %	**79.8 %**

FEV_1= Forced Expiratory Volume in 1 second; 6MWD=Six-minute walk distance; DL_{CO} =Diffusing Capacity of Lungs for Carbon Monoxide; RA_{950} =Relative Area < -950HU; **LRE** = Long run emphasis and **RP** = Run percentage.

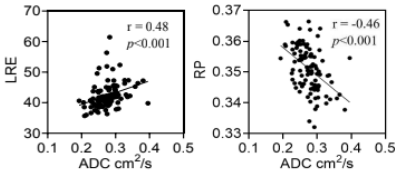

Validation of Advanced Approaches for Microstructural Diffusion MRI

Naila Rahman, Kathy Xu, Arthur Brown, Corey A. Baron

Diffusion Tensor Imaging (DTI) is an MRI technique that is sensitive to brain microstructure by quantifying the diffusion of water molecules. However, DTI lacks the specificity to model microstructure, since the change in water diffusion can be caused by multiple factors, such as myelin loss and axon degeneration. In this project, we are going beyond conventional DTI, and using multiple advanced MRI scans which will be sensitive to microstructure in complementary ways. Oscillating gradient spin-echo (OGSE) DTI will be used to probe the structural disorder of tissue and microscopic fractional anisotropy (μFA) DTI will be sensitive to cell shape. By applying DTI at various oscillating gradient frequencies, we can probe microstructure at different spatial scales. In contrast to fractional anisotropy (FA) in conventional DTI, which is sensitive to crossing neuron fibers, μFA aims to quantify anisotropy independent of fiber orientation. The objective of this study was to implement and validate these advanced MRI protocols in a healthy mouse brain in-vivo. Mean DTI metrics, such as fractional anisotropy (FA) and mean diffusivity (MD), were calculated in the corpus callosum of the mouse brain. The MD increased as a function of the oscillating gradient frequency, which is expected behavior for hindered diffusion. The preliminary results validate the OGSE and μFA protocols, and show that μFA may have greater specificity than FA in detecting neuron damage (Figure 1). To our knowledge, this is the first in-vivo rodent study that combines both OGSE and μFA protocols in the same scan to enable microstructure modeling.

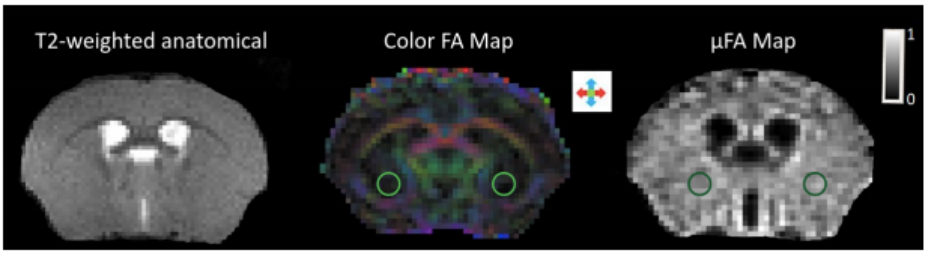

Figure 1: A color FA map and μFA map from a healthy mouse brain, indicating that gray matter regions (green circles) in the FA map are hypo-intense, compared to the μFA map.

Development of molecular imaging technologies for monitoring the fate of T cell immunotherapies

Veronica P Dubois, John J Kelly, Paula Foster, John Ronald

Chimeric antigen receptor (CAR) T cell therapy is an emerging cancer treatment showing remarkable success in patients with hematological malignancies using cancer-targeting T cells. Despite this success, CAR-T cells have the potential to cause severe side effects and are still showing incomplete treatment responses in some patients. An imaging tool for tracking CAR-T cells would provide important data on CAR-T cell fate that could help predict treatment response and potential for off-target toxicities. Our objective was to use fluorine-19 (19F) magnetic resonance imaging (MRI) to non-invasively track the fate of perfluorocarbon (PFC) labeled CAR-T cells in a mouse model of leukemia. NSG mice (n=6) received subcutaneous injections of 1x106 firefly luciferase expressing leukemia cells. After 21 days, mice were given intratumoural injections of 1x107 PFC labeled CAR-T cells (n=3) or saline (n=3). 19F MRI performed on days 1, 3, 7, and 11 post-CAR-T cell injection showed 19F signal in the tumours of treated mice and persistence of the signal at each timepoint. Bioluminescence imaging performed on days -1, 5, 8, and 10 post-CAR-T cell injection revealed that two out of three treated mice had decreased tumour burden by day 10 compared to day -1. For the first time, we have shown that PFC labeled CAR-T cells are cytotoxic in vivo and can be tracked over time using a 3T clinical MRI scanner. These cell tracking methods will aid in the optimization of CAR-T cell therapies and may be useful for evaluating CAR-T cell fate in patients.

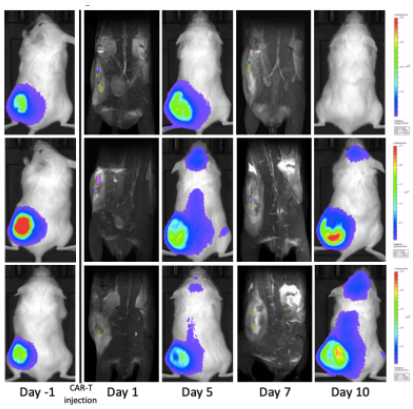

Figure 1: Bioluminescence imaging of tumour progression days -1, 5, and 10 post 19F perfluorocarbon labeled CAR-T cell injection and fluorine-19 MRI of 19F perfluorocarbon labeled CAR-T cells days 1 and 7 post-injection.

2. ORAL PRESENTATIONS (ROOM A)

2:00pm – 3:00pm

Brain Glutamate Measurement in a Triple Transgenic Model of Alzheimer's Disease

Dana N. Broberg, Dickson Wong, Miranda Bellyou, Alex Li, Marco Prado, Vania Prado, and Robert Bartha

Introduction: Decreased hippocampal glutamate has been reported in Alzheimer's disease (AD) using proton magnetic resonance spectroscopy (1 H-MRS). As the hippocampus is one of the earliest brain regions affected in AD, hippocampal glutamate may serve as a biomarker for early diagnosis. Recently, a triple transgenic knock-in App mouse model was developed that overcomes artificial phenotypes often observed in App mice. Here, our objective was to determine whether low hippocampal glutamate levels are a phenotype of this new triple transgenic mouse model as reported in human AD. We hypothesized that these mice would have decreased hippocampal glutamate relative to both single transgenic and control mice. Methods: Hippocampal glutamate/creatine levels were measured using 9.4 T 1H-MRS in six AppNL-G-F triple transgenic mice (15 months old) containing the Swedish (AppNL), Arctic (AppG), and Beyreuther/Iberian (AppF) mutations; three AppNL single transgenic mice; and four C57BL/6 mice. The MRS data were localized to a 6×3×3 mm3 voxel on the hippocampus (TR/TE=3500/100 ms). The effect of mouse model on glutamate/creatine was analyzed using one-way ANOVA. Results: One-way ANOVA showed that the effect of mouse model on glutamate/creatine was insignificant (F(2,10)=1.94, p=0.19) for AppNL-G-F (M=0.82, SD=0.11), AppNL (M=0.73, SD=0.10), and control mice (M=0.66, SD=0.16). Discussion: In this preliminary study, the AppNL-G-F triple transgenic mice did not exhibit decreased hippocampal glutamate levels relative to controls. However, the study is likely underpowered and more mice should be studied. Further investigation will be necessary to find a mouse model suitable for studying this biomarker of AD.

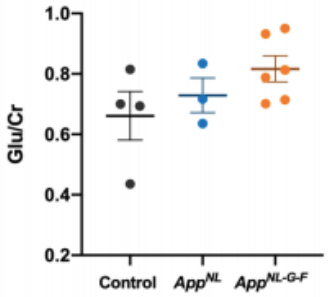

Figure 1. Mean glutamate/creatine (Glu/Cr) across mouse models (F(2,10)=1.94, p=0.19). Bars represent standard error of the mean.

An intrinsic registration method for ultrasound-guided breast lesion targeting under high-resolution positron emission mammography localization

Claire K. Park, J. Bax, L. Gardi, A. Fenster

Purpose: Targeting small, breast lesions with high accuracy is critical for diagnosis, treatment planning, and improving patient prognosis. We propose an integrated positron emission mammography (PEM) ultrasound (US)-guided breast biopsy workflow for enhanced functional target localization with real-time anatomical context to improve guidance. This work aims to validate a mechatronic system for PEM-US-guided breast biopsy. Methods: A mechatronic guidance system was developed to operate with an advanced PEM system. The system features a manually actuated mechatronic arm with ability to access the breast between PEM detector plates. The end-effector contains an integrated US transducer and biopsy needle focused on a remote-center-of-motion. Custom software was developed to track and display the biopsy needle. Guiding the needle to calibration fiducials on the simulated detector plate registered the coordinate systems using landmark-based registration. Validation was performed with fiducials within the targeting volume of a breast between detector plates. Fiducial Registration Error (FRE) and Target Registration Error (TRE) were quantified to evaluate accuracy. Principal component analysis assessed 3D directional trends within 95% confidence. Results: Calibration resulted in an FRE of 0.23 ± 0.20mm (N = 8) and TRE of 0.70 ± 0.20mm (N = 72). A prediction ellipsoid centered on the mean error, such that any future observation has 95% probability of targeting within the volume demonstrates the ability to target within a region < 2mm, in diameter. Conclusion: We demonstrate dynamic needle-tracking with sub-millimeter targeting error within the region of a breast between simulated PEM detector plates. When localized with PEM, our system demonstrates high targeting accuracy as a novel means toward image-guided biopsy.

Understanding muscarinic-mediated signaling in astrocytes using DREADDs for the control of neuroinflammation and cognition

Alycia M. Crooks, A. E.A. Hogan-Cann, L. M. Saksida, T. J. Bussey, V. F. Prado, and M. A.M. Prado

Astrocytes respond to neuronal activity and are necessary for plasticity, memory, and glial-neuron cross-communication. Astrocytosis leads to biochemical and morphological changes that may induce harmful neuroinflammatory processes. Thus, astrocytes play important roles in different cognitive processes and the modulation of neuroinflammation. Acetylcholine (ACh) regulates multiple cognitive processes and recent observations suggest that ACh can regulate hippocampal function in part by signaling in astrocytes. Both astrocytes and neurons express muscarinic receptors, thus astrocyte muscarinic receptor function in vivo is still not fully understood. We hypothesize that activating muscarinic receptors modulates astrocyte activity and leads to changes in neuroinflammation and cognition. We generated mice expressing either Gq (hM3Dq) or Gi (hM4Di) Designer Receptors Exclusively Activated by Designer Drugs (DREADDs), both of which are derived from muscarinic receptors (M3 and M4, respectively). These DREADDs no longer respond to their endogenous ligand ACh but are instead activated by Clozapine N-Oxide (CNO) in doses that do not affect other receptors. We have confirmed that in both hM3Dq and hM4Di mice, DREADDs are expressed specifically in astrocytes. Activation of hM3Dq in cultured primary astrocytes, by CNO, increased intracellular Ca2+. Interestingly, acute activation of hM3Dq in mice, by intraperitoneal injection of CNO, increased expression of proinflammatory cytokines in the cortex. Activation of global astrocyte Gi or Gq receptors do not cause significant changes on motor activity or anxiety-like behavior. Future experiments will assess cognitive function using touchscreen technology as well as neuroinflammation with acute and chronic activation of hM3Dq or hM4Di receptors.

Parametric Design of Focussed Collimator for Real-Time Intra-Operative Gamma Detection

Sydney Wilson, Hristo N. Nikolov, Rob Stodilka, Santiago Cobos, David W Holdsworth

Introduction: During breast cancer surgery, it is critical for a surgeon to excise a tumour with clean margins to prevent reoccurrence. Radiation emitting labels have made it possible to intraoperatively locate tumour cells, however, existing gamma probes lack the spatial resolution required to assess tumour margins. Objective: Design and fabricate a focussed gamma collimator (FGC) with high sensitivity that could accurately detect gamma radiation from a small region of interest. Methods: The FGC is a close packed hexagonal collimator that is focussed to a point 35 mm below the collimator face. To maximize collimator efficiency, the septal walls were tapered in proportion to the scaling factor of the focal point. The FGC was 3D printed using laser powder-bed fusion in both cobalt-chrome and tungsten alloy. The FGC was fitted to a Ludlum 44-2 Geiger counter. Using a precision x-y stage, an Americium-241 source (60 keV gamma photons) was translated in 0.5 mm increments under the FCG. Results: The FGCs were successfully manufactured using 3D metal printing to have a geometric transmission efficiency of 72%. A point spread function for the tungsten collimator determined the full width at half maximum resolution was 3.8 mm. Conclusions: Advancements to techniques in 3D metal printing made it feasible to fabricate a highly focussed collimator with a resolution that is four- times greater than existing gamma probes [1]. The unique ability of the FGC to collimate at a distance allows for future integration with ultrasound imaging to provide a complete, real-time, intraoperative image guidance system.

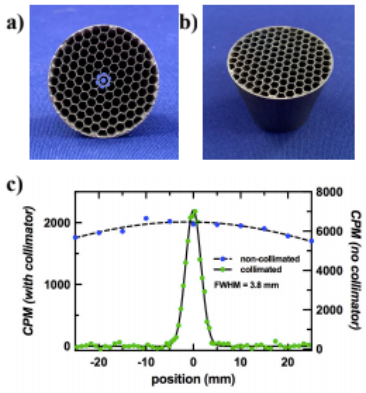

Fig. 1: (a) Top view of cobalt-chrome FGC. (b) Isometric view of tungsten FGC. (c) Point spread function of non-collimated and tungsten collimated counts per minute over a low activity Americium-241 source.

In vivo molecular imaging of the cholinergic projection system in mice

Kate M. Onuska, Hayley Shanks, Jonathan Thiessen, Robert Bartha, Taylor W. Schmitz, Marco AM. Prado

Evidence suggests that denervation of cholinergic neurons arising from the basal forebrain is one of the earliest neurobiological indicators of Alzheimer's disease. However, there is currently no standardized method to measure both when and where these deficits first occur in the brain. The recent development of the PET radiotracer [18F] FEOBV may help to overcome this obstacle. [18F] FEOBV selectively binds to VAChT, a protein found solely in the presynaptic terminals of cholinergic neurons. Given this, we will perform the first study to investigate the sensitivity and specificity of [18F] FEOBV using mouse lines with genetically modified expressions of VAChT. Because [18F] FEOBV had yet to be used in mice, our first objective was to characterize the binding intensity and uptake profiles of this tracer in wild type mice. To do so, we collected both structural magnetic resonance images from the 9.4T scanner at Robarts Research Institute, as well as dynamic PET data of [18F] FEOBV at the Lawson Health Research Center in male and female wild type mice (n=2; age=3 m.o.). Our pilot experiment confirmed that maximum binding intensities of [18F] FEOBV are anatomically localized to brain regions known to receive cholinergic innervation, including the striatum, the hippocampus, and the thalamus. Moreover, time activity curves created from a 90-minute dynamic microPET scan revealed robust increases in [18F] FEOBV uptake specifically in these same cholinergic regions relative to non-cholinergic areas. Overall, these preliminary results support the calibration of [18F] FEOBV using mice to determine its eligibility as a clinical tool.

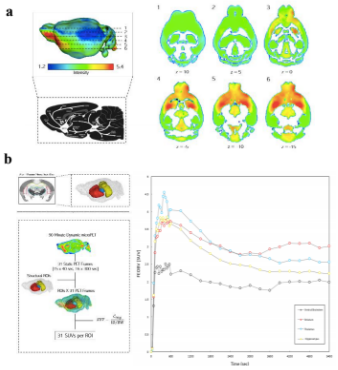

Figure 1. Average binding intensity and uptake profiles of [18F] FEOBV in wild type mice (n=2, male: female). (a) [18F] FEOBV binding intensity distributions displayed on six superior-inferior axial slices. Maximum binding intensities (indicated by warmer colours) are localized to brain regions that receive cholinergic innervation. (b) Standard Uptake Values (SUVs) from a 90-minute microPET scan with [18F] FEOBV in three cholinergic ROIs (striatum=red, thalamus=blue, hippocampus=yellow). Relative to areas that do not receive cholinergic input (ventral brainstem=black), SUVs of [18F] FEOBV in these three ROIs are consistently higher across the entirety of the 90-minute scan.

Intraoperative visualization of intracavitary gynecologic brachytherapy applicators using 3D transrectal ultrasound

Jessica R. Rodgers, Lucas C. Mendez, Douglas A. Hoover, Jeffrey Bax, Vikram Velker, David D'Souza, Aaron Fenster

Purpose: To assess three-dimensional (3D) transrectal ultrasound (TRUS) for visualizing intracavitary gynecologic internal radiotherapy (brachytherapy) applicators, including ring-andtandem (R&T) and tandem-and-ovoids (T&O), providing the potential for intraoperative evaluation and TRUS-planned first treatment, particularly in healthcare cost-constrained settings. Methods: As a proof-of-concept, we imaged four patients undergoing intracavitary gynecologic brachytherapy, including one with an R&T applicator and three with T&O applicators. The ability to visualize critical features for evaluation/planning, including the central tandem, ring or ovoids, uterus/cervix, tumour, and rectal wall, was qualitatively assessed. Results: The uterus, rectal wall, and posterior wall of the ring in the R&T applicator were visualized (Fig. 1); however, the ring produced a large shadowing artefact. This obscured anterior and central features, such as bladder and cervix, and prevented complete reconstruction of the applicator, which is required for treatment planning. The T&O applicators were more clearly visualized (Fig. 2) than the R&T applicator, with less shadowing, and allowed identification of all necessary anatomical structures, particularly the vagina, cervix, uterus, tumour, bladder, and rectal wall. Conclusions: Intraoperative visualization using 3D TRUS has the potential to provide an accessible approach to verifying applicator placement and assessing relevant anatomy, particularly in the context of resource-constrained settings. Future work will broaden the study cohort for more comprehensive analyses of structure identification and incorporation of transabdominal ultrasound to overcome the challenges with imaging R&T applicators.

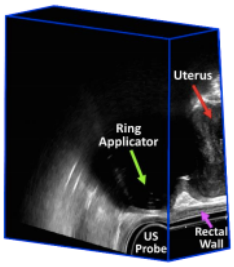

Figure 1. Patient image with a ring-and-tandem applicator.

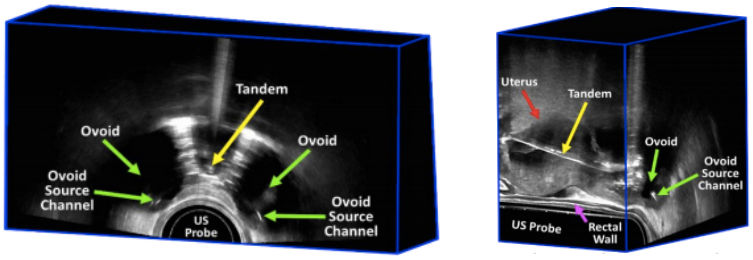

Figure 2. Two patient images showing tandem-and-ovoids applicators, demonstrating clear visualization of both the applicator and nearby anatomy.

Investigating stroke origin from thrombus cellular composition

Emily Qin, Spencer Christiansen, and Maria Drangova

Introduction: Stroke is the 3rd leading cause of death in Canada, with the most common origin of stroke clots being cardioembolism (CE) and large artery atherosclerosis (LAA).Understanding differences in the acute presentation of these two groups will ultimately lead to better patient care by optimizing treatment and preventing recurrent stroke. Histological analysis of CE and LAA clots may provide valuable information towards differentiating stroke etiologies. Methods: Patients who had strokes of CE (n=31) and LAA origin (n=9) had thrombi removed via mechanical thrombectomy. These thrombi were placed on microscope slides and stained using hematoxylin and eosin (H&E) to view red blood cells (RBC), white blood cells (WBC), and fibrin content. On ImageJ, the three cell types of interest were segmented according to their distinct colouring following H&E staining (Figure 1). After colour segmentation, the cell proportions of RBC, WBC, and fibrin were quantified using a MATLAB code. Results: The average proportion of RBC, fibrin and WBC content in CE and LAA thrombi are shown in Figure 2. For both etiologies, RBC and fibrin cells dominated, together constituting over 99% of the thrombus cellular composition. CE thrombi had lower RBC and higher fibrin content than LAA thrombi. Conclusions: Consistent with previous studies, LAA thrombi had 4.03% higher RBC content than CE thrombi. Future developments of this project should consider larger sample sizes, especially for LAA samples.

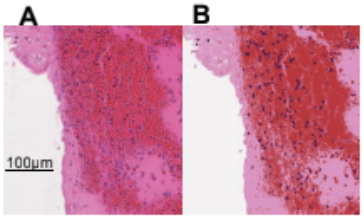

Fig. 1: Representative thrombus (A) H&E section and (B) segmentation output at 20x magnification (red: RBC, pink: fibrin, blue/black: WBC).

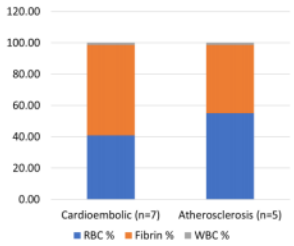

Fig. 2: Average proportion of RBC, fibrin, and WBC content in CE (n=31) and LAA (n=9) thrombi.

Spinal Cord Compression Severity Leads to Cortical Reorganization in Patients with Cervical Spondylotic Myelopathy

Alicia Cronin, Sarah Detombe, Neil Duggal, Robert Bartha

Introduction: Cervical spondylotic myelopathy (CSM) is a degenerative disease of the spine that causes compression of the spinal cord leading to neuronal injury due to hypoxia. Neuronal injury in CSM can produce functional deficits and cortical reorganization. Unfortunately, direct in-vivo measurement of the extent of hypoxia is not currently available in the spinal cord due to technical challenges, forcing the use of proxy measurements such as spinal cord compression. Thus, the objective of this study was to determine if the severity of spinal cord compression was associated with functional brain activity measured using task-based fMRI. Methods: A 3.0T Siemens Prisma Fit MRI scanner was used to acquire functional images of 23 CSM patients (14 men, mean age (±SD) 65±14.5 years) while performing a right-handed finger-tapping task. Volume of activation (VOA) and % BOLD signal were determined using region-of-interest analysis. To determine severity of compression, semi-automatic segmentation of the spinal cord was performed, and total compression volume was found. Results: There was a significant correlation between compression volume in the spinal cord and the contralateral primary motor cortex VOA (p=0.03, r=0.45) and % BOLD signal (p=0.005, r=0.56), shown in Figure 1. Conclusion: CSM patients with severe compression of the spine also have the largest activation of their primary motor regions. It is possible that the increase in activation is due to cortical reorganization to minimize functional deficits. Future studies to measure hypoxia at the site of compression may provide more insight into the mechanisms of neuronal injury in CSM patients.

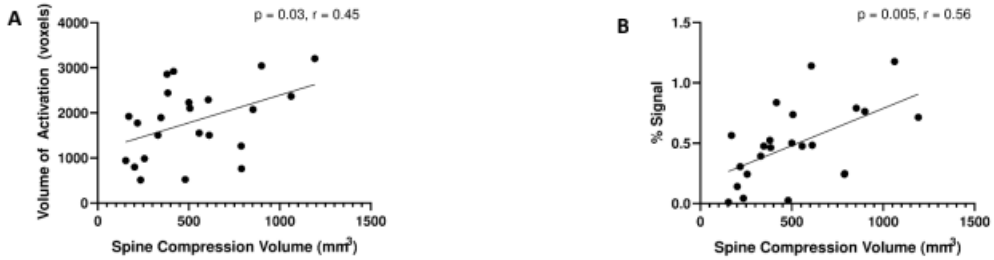

Figure 1: A: Relationship between VOA of contralateral M1 and compression volume B: Relationship between % BOLD signal of contralateral M1 and compression volume

Evaluation of a mixed-reality first person point of view needle navigation system

Leah Groves, Natalie Li, Terry Peters, Elvis Chen

Introduction: Millions of Central venous catherizations (CVC) are performed annually, with the internal jugular vein (IJV) being the most common insertion site. Carotid artery (CA) puncture can occur in upwards of 7.8% of ultrasound (US) guided CVCs at the IJV. We hypothesize that aligning the visual and motor fields will improve targeting accuracy in the needle insertion required for CVC. Methods: A surgical navigation system was developed as depicted in Fig.1. This system was visualized on a monitor and within the HTC VIVE Pro head-mounted display (HMD) and compared to US-only guidance. A phantom that mimics the appearance of the IJV and CA under US was developed. All 33 clinical practitioners performed one needle insertion for each system (HMD, screen and US-only) in the phantom. The insertion success and the distance from the final needle tip position to the closest point on the vessel wall were calculated. Conclusions: The use of a HMD to align the visual and motor fields improved needle navigation. The HMD system had a success rate of 94% compared to 64% for the US-only method. Clinicians also more consistently targeted the center of the vessel, with an average distance from the final needle tip position to the center wall of 3.8 mm and 2.2 mm, for the HMD and US-only systems respectively. This work promotes the benefits of first person perspective and the use of HMDs for surgical navigation research.

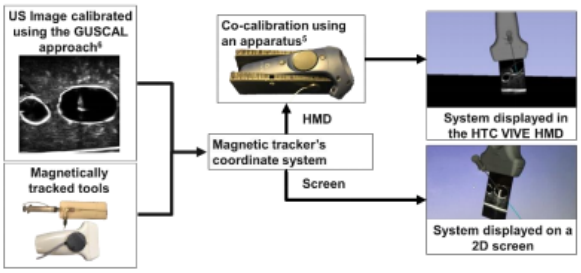

Fig. 1: Flow chart depicting the development of the advanced surgical navigation system

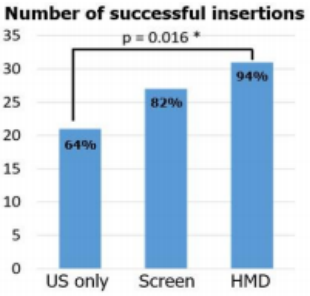

Fig. 2: Number of successful insertions by modality

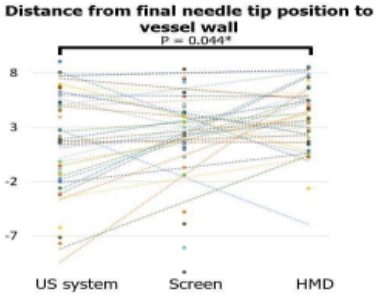

Fig 3. Distance from the final needle tip position to the closest point on the vessel wall by modality. Each colour represents a user.

Integration of tactile information from multiple fingers in human primary sensory cortex measured using high-resolution fMRI

Spencer Arbuckle, Andrew Pruszynski, Jörn Diedrichsen

Sensory information across fingers is integrated to yield a percept of an object in the hand. Within human primary sensory cortex (S1), Brodmann areas (BA) 3a and 3b receive sensory input in a finger-specific fashion. These areas then project to BA1 and 2, which are hypothesized to integrate information across fingers. How this integration occurs is unknown. To study this in humans, we used functional magnetic resonance imaging (fMRI, 7T, 1.4mm3) to measure activity patterns evoked in left S1 during passive single- and multi-finger stimulation of the right hand. In 3a, finger encoding and overall activity was weakest, likely because this area largely receives proprioceptive input. In BA3b, 1, & 2, clear encoding for fingers was found, and activity increased with the number of stimulated fingers. Voxel activity in 3b was more selective to specific fingers compared to voxels in BA1 and 2, indicating larger overlap of finger representations in BA1 and 2. We investigated if this overlap reflected a unique integration of sensory information across fingers. For each subregion, we fit a linear model where multi-finger activity patterns were predicted as the sum of the constituent single-finger patterns. To account for local inhibition, each pattern was scaled by a constant dependent on the number of fingers stimulated. This linear-nonlinear model could well account for the representations in all subregions of S1, indicating that at the resolution of fMRI, passive sensory information each finger is linearly integrated in S1.

Using fluorine-19 MRI cell tracking to detect and quantify peripheral blood mononuclear cells and regulatory T cells in vivo

Olivia C. Sehl, C. Fink, K.N. MacDonald, M.K. Levings, G.A. Dekaban, P.J. Foster

Cell-based immunotherapy refers to administration of immune cells for the treatment of an ever- increasing list of cancerous, autoimmune, degenerative, and infectious diseases; some of which are rare and/or difficult to treat. Peripheral blood mononuclear cells (PBMC) are FDA approved for prostate cancer and regulatory T cells (Treg) are under development to replace drug-induced immunosuppression. Migration of administered cells to secondary lymphoid tissues is essential to elicit adaptive immune responses. It is crucial to know whether the cells have migrated to lymph nodes and in what quantity. Fluorine-19 (19F) MRI is a technique used to detect and quantify perfluorocarbon- (PFC)-labeled cells. Our objective is to conduct longitudinal cell tracking of human PBMC and Treg in immunocompromised mice using 19F MRI at 3T, to study cell migration, persistence, and quantity in vivo. PFC+ PBMC were injected into Nu/Nu mice footpads (9x106 cells total, n=4) or by intraperitoneal injection (5x106 cells, n=2). In another cohort, 10x106 PFC+ Treg and 10x106 unlabeled PBMC were administered intravenously (n=4) or subcutaneously (n=4). 24 and 48 hours later, 1 H/19F images were acquired on a 3T clinical MRI using a dual-tuned surface coil and 3D bSSFP sequence. 19F images show the accumulation of PFC+ PBMC/Treg in the popliteal, inguinal, and axillary lymph nodes. The number of cells were quantified at each node. Images suggest that the route of cellular administration may impact the treatment efficacy. This is the first study to conduct in vivo 19F imaging of Treg and the third 19F cell tracking mouse study at 3T.

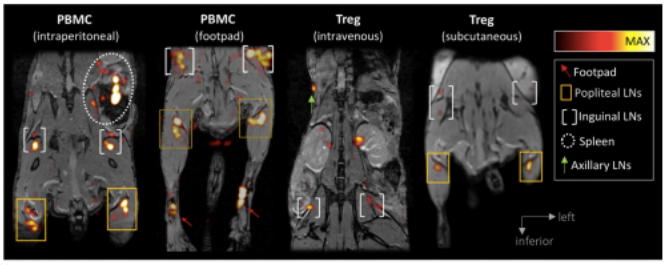

Figure: 19F/1 H MRI overlay of mice showing detection of PFC+ PBMC after intraperitoneal or footpad injections and PFC+ Treg after intravenous or subcutaneous injections. PFC+ cells accumulate in popliteal lymph nodes, inguinal lymph nodes, the spleen, and axillary lymph nodes (see legend). Images were acquired both 24 and 48 (not shown) hours post-adoptive transfer. The colour scale bar represents 19F spins.

Motivation and cue-directed effort are regulated by acetylcholine/glutamate co-transmission from striatal cholinergic interneurons

Ornela Kljakic, Helena Janickova, Miguel Skirzewski Prieto, Monica S. Guzman, Sara Memar, Salah El Mestikawy, Yulong Li, Lisa M. Saksida, Timothy J. Bussey, Vania F. Prado, Marco A.M. Prado

In the striatum, cholinergic interneurons (CINs) co-express the vesicular acetylcholinE (ACh) transporter (VAChT) and vesicular glutamate (Glu) transporter 3 (VGLUT3) and thus can store and release ACh and Glu. These two neurotransmitters seem to regulate dopamine in different ways, and they can distinctly impact striatal-dependent behaviours. In this study, we altered ACh and/or Glu secretion from CINs in mice to examine their role in motivation. Using different touchscreen-based motivation tasks, we found that mice with an individual deletion of ACh or Glu release (selectively knocked out VAChT or VGLUT3, respectively, in the striatum), exhibited minor changes in motivated behaviour. In contrast, mice in which both VAChT and VGLUT3 were deleted, were initially slower in completing motivation tasks, but gradually, increased their performance and were willing to exert more effort to obtain rewards. VAChT/VGLUT3 double-KOs were less capable of responding to the correct stimulus, suggesting a misplacement of their effort. Given the reciprocal interaction between CIN neurotransmitters and dopamine release, we tested the sensitivity of performance to the D2 antagonist haloperidol. Interestingly, the performance of control mice was impaired by haloperidol, whereas the double-KO mice were unaffected. Furthermore, we found that dopamine dynamics were altered in our mouse lines with VAChT-deficient and VGLUT3-deficient mice having decreased and increased levels, respectively. In conclusion, the present study indicates that individually, ACh and Glu released by CINs play subtle roles in motivated behaviour. However, synergistic signalling by these two neurotransmitters is required for mice to target their efforts in solving different motivation-related touchscreen tasks.

"Lone" Atrial Fibrillation is Primarily Polygenic

Julieta Lazarte, Jacqueline S. Dron, Adam D. McIntyre, Zachary Laksman, Robert A. Hegele, Jason D. Roberts

Background: "Lone" atrial fibrillation (AF) defines a subset of AF patients diagnosed early in life and with no clinical evidence of cardiopulmonary disease. AF is understood to have both monogenic and polygenic disease determinants; further "lone" AF is considered to have a greater genetic burden. However, our understanding of its molecular basis remains incomplete. Methods: DNA was genotyped from 186 adult "lone" AF patients of European ancestry and all analysis were compared with two reference groups. DNA microarray data were imputed using the Michigan Imputation Server. Utilizing custom python scripts, 6,730,541 and 1,168 common variants were calculated into polygenic risk score (PRS) as reported by Khera et al. (2018) and Weng et al. (2018), respectively. The distribution of the two PRS were compared using GraphPad Prism. Results: A total of 34.4% of "lone" AF patients were in the top 90th percentile of Khera's PRS and 26.3% of Weng's PRS, while only 10% of controls for both scores. The area under the curve was75.9% for Khera's and 70.0% for Weng's PRS. Considering Weng's PRS, "lone" AF patients were 3.16 times (95% CI [2.01-4.98]; P < .0001) more likely to have an inherited polygenetic susceptibility for AF compared with controls. Conclusion: Canadian patients with "lone" AF carry a significant burden of common variants that increase their susceptibility for AF. Our findings provide a novel exploration of two validated AF PRS in a Canadian "lone" AF cohort. In fact, the performance of the AF PRS were comparable, making the 1,168 a practical option for this population.

Development of Iron Oxide Nanoparticles for Magnetic Particle Imaging

Julia Gevaert, Paula Foster

Magnetic Particle Imaging (MPI) is an emerging imaging modality capable of tracking cells in- vivo. This modality is unique by its direct detection of superparamagnetic iron oxide nanoparticles (SPIOs) with positive contrast. The signal generated from these particles is linearly correlated with iron content, enabling a quantification method that is both sensitive and specific. Tracer development is a key influencer in MPI, since they are the sole contributors of signal. Therefore, an understanding of the magnetic relaxation of particles in MPI is necessary for selecting the ideal particle properties. Relaxometer testing measures the full magnetic response of a particle for MPI, creating a point spread function with peak amplitude as a measure of sensitivity, and peak FWHM as a measure of resolution (Figure 1). In this study, nanoparticles developed for MPI were analyzed using relaxometer data. Relative resolutions and sensitivities were measured for each particle and compared with their respective properties, including core size and chemical coating. The results from this study provide useful information on optimal particle properties. While this information is useful for understanding the basic behavior of particles in MPI, there must also be utility for in- vivo applications. Future work will focus on translating these particles to cell tracking applications by testing cell labeling techniques and evaluating in-vivo tracer performance.

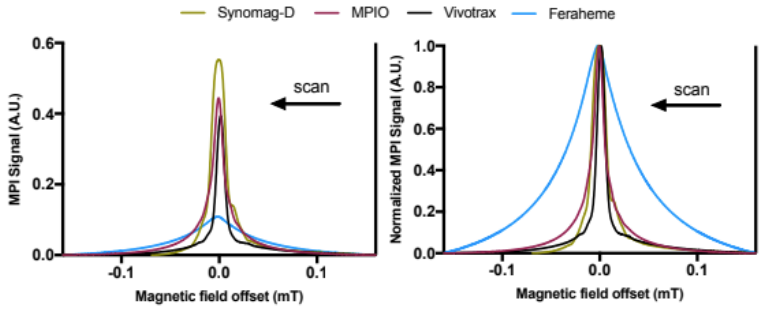

Figure 1: Relaxometer data for Synomag-D, MPIO, Vivotrax, and Feraheme, four commercially available nanoparticles for MPI showing (A) particle sensitivity, shown by relative peak amplitudes normalized to iron content (B) particle resolutions, shown by peak FWHM.

Plasma phosphatidylcholines are associated with the longitudinal grey-matter integrity of the basal forebrain

Hayley R.C. Shanks, Kate M. Onuska, Taylor W. Schmitz

The basal forebrain is the major source of cortical cholinergic innervation, which is vital in modulating several cognitive functions. In Alzheimer's disease (AD), cholinergic neurons from the basal forebrain degenerate before other neurotransmitter systems and before the appearance of cognitive deficits. However, current understanding of the cause of this selective vulnerability is limited. One theory posits that the cholinergic basal forebrain is vulnerable to neurodegeneration because it requires choline-containing compounds, such as phosphatidylcholines, for both acetylcholine biosynthesis and membrane support. To test this theory we leveraged the Alzheimer's Disease Neuroimaging Initiative (ADNI) dataset. ADNI contains structural magnetic resonance imaging data, cerebrospinal fluid (CSF) biomarkers of amyloid beta and tau, and plasma lipidomics in AD patients, as well as neurotypical older adults. We hypothesized that phosphatidylcholines are dysregulated in AD, and thus will be associated with longitudinal volumes of the basal forebrain. Participants were separated into normal or pathological CSF groups based on the presence of amyloid and tau in their CSF. First, we demonstrate that only one cluster of lipids – unsaturated phosphatidylcholines – are altered by pathological CSF (p = 0.001). Then, using a form of multivariate pattern analysis called partial least squares correlation, we show that unsaturated phosphatidylcholines are significantly associated with longitudinal grey matter degeneration of the basal forebrain (p = 0.001), and that this relationship is modified by the presence of pathological CSF. Overall, this study provides the first in vivo evidence for a relationship between phosphatidylcholines and the basal forebrain, supporting a longstanding theory in cholinergic research.

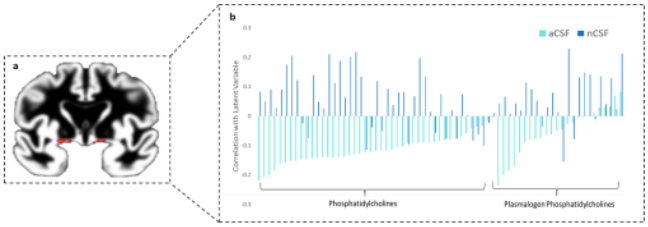

Figure 1. A single latent variable (p = 0.001) derived from partial least squares correlation describes the joint contribution of unsaturated phosphatodylcholines onto longitudinal grey matter degeneration within the basal forebrain. (a) Voxels within the basal forebrain that are significantly associated with plasma phosphatidylcholines through the latent variable are shown in red. (b) The correlation between plasma phosphatidylcholines and the latent variable differs by the presence of pathological CSF. aCSF = abnormal (pathological) cerebrospinal fluid (teal), nCSF = normal cerebrospinal fluid (blue).

Automatic determination of the regularization weighting for wavelet-based compressed sensing MRI reconstructions

Gabriel Varela-Mattatall, Corey A Baron, Ravi S Menon

Compressed sensing reconstruction demands a correct regularization weighting for its optimization problem. Nonetheless, most procedures to defined it are based on iterative testing and/or comparisons with an unreal fully-sampled image. Here, we present a technique that automatically determines the regularization weighting for wavelet-based compressed sensing reconstructions. Our proposal determines level-specific regularization weighting factors by applying statistics about the noise in the wavelet domain from the zero-filled image. We compare reconstruction results obtained by our technique to estimate the regularization weighting to the ones obtained by the L-curve and the minimum normalized mean squared error. Then, we characterize the behavior of our technique to different mother wavelets and its reconstruction performance to different noise levels and under-sampling patterns using simulations. Finally, we show results for different MRI techniques and/or contrasts. Our proposal provides comparable reconstructed image quality to that obtained by the regularization weighting obtained by either L-curve or NMSE for a certain range of noise levels and under-samplings factors. Overall, our main finding is a rapid, automatic and robust procedure to determine the regularization weighting. The impact of our research is that our finding enables prospective tuning-free wavelet-based compressed sensing reconstructions.

Figure 1. General scheme. This proposal emerges from the interaction between proximal algorithms, denoising and wavelets. Our main finding is a rapid and automatic procedure to determine the regularization weighting for wavelet-based compressed sensing reconstructions. Therefore, no iterative testing for determining the regularization weighting and no comparisons with an unreal fully-sampled image.

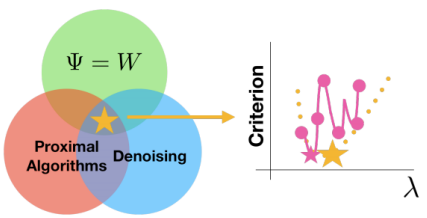

Single Cell RNA Sequencing

Wu, Yutong., Abdelhady, A., Biltcliffe, J., Carter, D.E., Robinson, J.F., Hegele, R.A.

Bulk RNA sequencing (RNA-Seq) is one application of Next Generation Sequencing (NGS) which revolutionized genomic research with its sequencing depth, high throughput data, and ability to measure gene expression of complex transcriptomes. Single-cell RNA sequencing (scRN-seq), as the name implies, enables RNA sequencing of induvial cells and allows visualization of various cell types within a tissue or cell mixture. The 10X Genomics Chromium Next GEM Single Cell 3' assay measures all eukaryotic poly-A-tailed RNA at the single-cell level. Starting with single cells in suspension, the 10X Chromium Controller combines single cells, Gel beads EMulsion (GEM) beads with Unique Molecular Identifiers (UMI) and reagents into oil droplets. Cell lysis and reverse transcription then occur in each of the droplets, resulting in barcoded cDNA. Partitioning oil is then removed to break the droplets, allowing barcoded cDNA to be amplified, indexed and sequencing on Illumina platforms. Resulting data is analyzed by a set of pipelines, starting with demultiplexing and FASTQ generation, reference genome alignment, UMI deduplication, normalization, statistics and filtering to only include informative genes. Next, Principal Component Analysis (PCA) is performed to reduce data dimensionality. Visualization is then achieved using t-SNE and UMAP algorithms, in which the latter provides meaningful insight on inter-cluster relations. Filtered gene lists are subjected to hierarchical clustering, which generates heatmaps to present differential gene expression and reveal cellular heterozygosity of the tissue. The London Regional Genomics Center (LRGC) now provides this leading-edge technology and single cell data analysis to the local scientific community.

Micro-computed Tomography Determination of the Relationship Between Visceral Adipose Tissue and Whole-Body Adipose Tissue in Rats and Mice

Joseph U. Umoh, A. Burke, E. Turley, C. Norley, S.I. Pollmann, J. Dunmore-Buyze, T. Appleton,3 M. Drangova, M. Huff, and D.W. Holdsworth

Background: Clinical research in adipose tissue and obesity often begins in rat and mouse models. In this study, the masses of visceral adipose tissue (VAT) in the abdominal cavity and whole-body adipose tissue (WAT) were measured from micro-computed tomography images of rats and mice (Fig.1). While WAT measurement is easily automated, VAT requires manual segmentation and is time consuming. Objectives: Our objectives are to determine a relationship between VAT and WAT in rat and mouse models and to investigate whether the relationship is different in the male and female of both animals. Methods: Masses of WAT and VAT in 91 rats and 80 mice (male and female) were computed using adipose tissue density1 of 0.90 g cm-3 and image threshold values of between -380 and -30 HU. Results: Linear regression analysis showed that VAT = a WAT - b, for both rats and mice (Fig. 2), where a and b are constants. For rats ar = 0.43 ± 0.01, br = 8.96 ± 1.19 and for mice am = 0.35 ± 0.01, bm = 0.71 ± 0.10. For both animals R2 = 0.97 and $p<0.0001$. The root-mean-square error was 3.1 g for rats and 0.2 g for mice. The regression slopes were significantly ($p<0.05$) different in male and female of both animals. This is consistent with the study that showed that normal male mice of the same age as females tend to weigh more than females. Conclusions: This study determines a linear relationship between the visceral and whole-body adipose tissue for rats and mice. It shows that the equation parameters are different for male and female in both animals. These formulae could be used to easily estimate the mass of visceral adipose tissue using whole-body adipose tissue, in male and female of both animals.

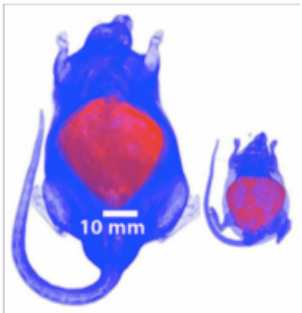

Fig. 1: Micro-CT image-rendering of a whole-body (face-up) rat (left) and a mouse (right) showing the mass of visceral adipose tissue (red) and the rest of the adipose tissue (blue).

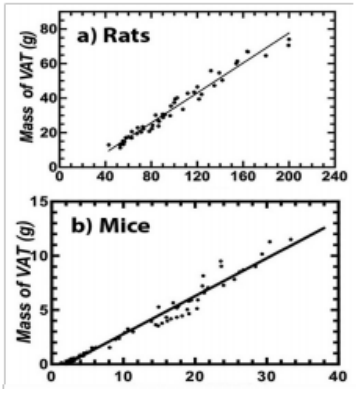

Fig. 2: Plot of the mass of the whole-body adipose tissue (WAT) against the mass of the visceral adipose tissue (VAT) showing the linear regression line for (a) rats and (b) mice.

Deep learning prediction of stroke thrombus RBC content from multiparametric MRI ex vivo

Spencer D. Christiansen, Junmin Liu, and Maria Drangova

Introduction: The proportion of red blood cell (RBC) content in stroke thrombi is associated with valuable clinical parameters including stroke etiology and responsiveness to thrombectomy therapy. Thrombus RBC content is currently determined retrospectively through histological examination. Previous work showed that MR R2* and quantitative susceptibility mapping (QSM) values were sensitive to porcine clot RBC content in vitro; this study examines the feasibility of applying deep learning to multiparametric MR images for predicting RBC content in human stroke thrombi ex vivo. Methods: 48 acute stroke thrombi retrieved via thrombectomy procedures were MR scanned and fixed in formalin for histological examination. Thrombi were imaged at 3T using a custom dual echo-train 3D GRE sequence to produce magnitude images, R2* and QSM maps. Thrombus histological sections were H&E stained to determine RBC content. A 3-layer convolutional neural network (CNN) implemented in Matlab was trained to predict RBC content from segmented multiparametric MR image slices. Different network parameters and data augmentation techniques were tested, as detailed in Table 1. Average accuracy (predictions within 10% of histology) and absolute error across 8-fold cross validation experiments assessed network performance. Results: Average accuracy and absolute error of the top-5 performing networks at each data augmentation level are shown in Figure 1. Accuracy and absolute error improved from 65±1% and 8.6±0.2% in the original data set up to 71±1% and 8.1±0.2% after augmentation. Conclusion: The CNN learned to predict stroke thrombus RBC content from multiparametric MR images with reasonable accuracy when applying augmentation, despite a limited data set.

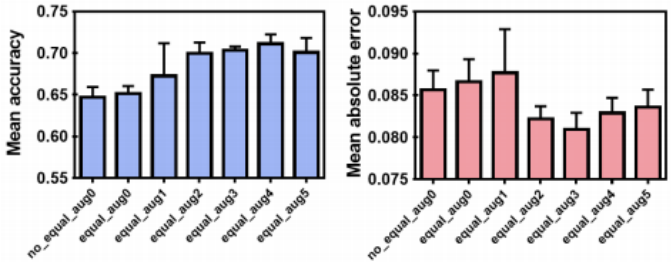

Fig. 1: Mean accuracy (A) and absolute error (B) of the top-5 performing network implementations at each data augmentation level. (equal = input sampling equalization, aug0 = no augmentation, augX>0 = random augmentation of X duplicates of the training set)

Network parameters		Augmentation parameters	
Optimizer	Adam	Scale range	(0.7, 1.3)
Learning rate	0.001	Translation max	5
Regularization factor (L2)	0.01	Rotation range	(-90°, 90°)
Training epochs	[4,5,6,7,8,9]	Shear range	(-30°, 50°)
Batch size	[6,8,12]	Duplication factor	[1,2,3,4,5]
Dropout	[0,0.1,0.2,0.3,0.4]	Input equalization	[T,F]

Table 1: Parameters used for network evaluation. ([tested network implementations])

Monitoring a patient derived xenograft model of breast cancer with magnetic particle imaging and bioluminescence imaging

Natasha N. Knier and Paula J. Foster

Introduction: Recently, there is momentum towards utilizing patient-derived xenograft (PDX) models to better reflect breast cancer tumour properties observed clinically. Magnetic particle imaging (MPI) is a novel technology for cancer cell tracking and quantification of iron that we complement with bioluminescence imaging (BLI), which measures cellular viability. We report the first iron-labeling and multimodal imaging of PDX breast cancer cells. Methods: Luciferase expressing PDX cells (F2-7) were labeled with micron-sized paramagnetic iron oxide nanoparticles (MPIO), confirmed with Perl's Prussian Blue (PPB). 2x105, 6x105 and 1x106 F2-7 cells were seeded for BLI. NOD/ SCID/ILIIrg-/- (NSG) (n=2) mice received injections of 1x106 iron-labeled F2-7 cells into the fourth mammary fat pad (MFP). BLI and MPI were performed longitudinally out to day 42 and signal was quantified. Ex vivo MPI of a labeled and unlabeled MFP tumour was performed. Results: PPB revealed successful iron labeling (81.80±10.14% efficiency). In vitro BLI showed a significant positive correlation between cell number and signal (R2=0.9664). Both in vivo BLI and MPI revealed signal from the MFP injected cells, increasing with tumor development. Ex vivo MPI showed signal from an iron-labeled MFP tumor and no signal from an unlabeled MFP tumor. Summary: We show the first successful iron-labeling of a PDX and the first application of MPI to monitor PDX MFP tumor growth. Longitudinal MPI with BLI revealed increasing iron content and proliferation of labeled PDX tumours. Our work demonstrates the critical role that multimodal cell tracking can play when studying breast cancer with a clinically relevant model.

Determining the relationship between early and rapid brain atrophy on clinical outcomes in refractory status epilepticus: a retrospective analysis

Nafis Anwar Hossain, Jason Tzu Chieh Kai, Teneille Gofton, Ali Khan

Background: The unremitting seizure activity of refractory status epilepticus (RSE) is known to mediate diffuse brain atrophy in RSE. However, acute patterns of brain atrophy in RSE (i.e. regional predominance, timing, rate) and their prognostic significance is poorly understood. Methods: We retrospectively identified RSE patients with at least 2 T1-weighted (T1w) MRI scans >4 weeks apart and extracted their clinical data. Serial volumetric analysis was done and baseline T1w scans at onset of RSE were compared to follow-up scans closest to 6 months apart. Measurements of ventricle-brain ratio (VBR) and subcortical gray (SG) volume were compared in that time interval; percent change of follow up to initial values were taken as ΔVBR and ΔSG. Clinical outcome was measured by Glasgow Outcome Scale (GOSE) and assessed for statistical association with volumetric parameters. Linear regression analysis was used to determine rate of generalized atrophy (RGA) and rate of subcortical gray atrophy (RSGA). Results: 8 patients met inclusion criteria. ΔVBR, ΔSG, and RGA were significantly negatively correlated with GOSE. Linear regression of aggregate VBR of RSE patients with a poor outcome (GOSE<5) had a strong correlation with days since onset (R=0.84); no correlation was observed for patients with best outcome (GOSE=5; R=0.005). The unfavourable outcome group had a significantly higher ΔVBR, ΔSG, RGA, and RSGA compared to the favourable outcome group. Conclusion: There appears to be a relationship between a greater extent of early generalized and subcortical gray atrophy, as well as a greater rate of atrophy with poor outcomes in RSE.

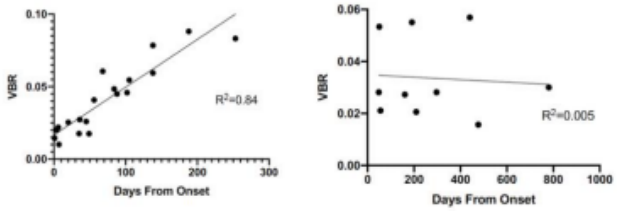

Fig. 1: Linear regression showing aggregate VBR change over time for patients with a GOSE of (a) <5 and (b) =5. Day zero represents time of onset of RSE.

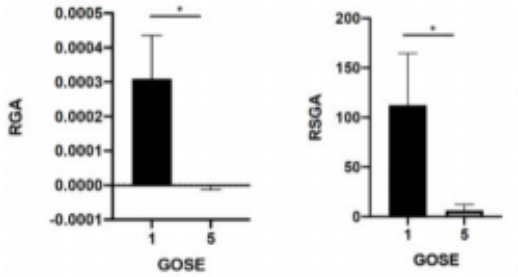

Figure 3: Comparison of RGA and RSGA for RSE patients with a GOSE of (a) 1 and (b) 5. Asterisks (*) indicate a statistically significant difference (p<0.05)

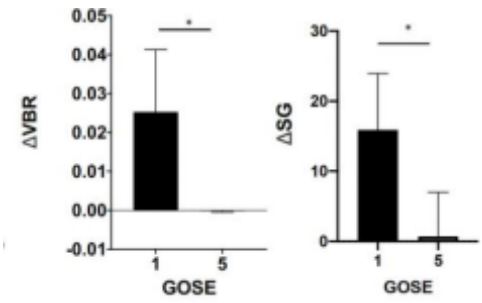

Figure 2: Comparison of change in VBR and change in SG for RSE patients with a GOSE of (a) 1 and (b) 5. Asterisks (*) indicate a statistically significant different (<0.05)

Prevention of new and recurrent breast cancer brain metastases using immune response-guided radiation therapy

Sawyer Badiuk, Jeff Chen, Eugene Wong

Background: Breast cancer is a terrible disease to be diagnosed with. The only thing worse is being told the cancer has spread to other parts of the body. With breast cancer, spreading typically occurs in the brain and is referred to as brain metastases. Cancer that has spread to the brain can be treated with surgery or radiation. This treatment is highly accurate, but may not stop cancer cells from growing. A preventative radiation treatment targeting these cells is needed, however along with stopping tumour growth, adverse cognitive effects are apparent. Irradiating the brain causes damage to the tissue, this is ideal for cancerous cells. The tissue damage kicks the immune system into action and causes inflammation. In short duration inflammation helps kill cancer cells, while long term can lead to undesirable cognitive side effects. Hypothesis: The conventional preventative treatment involves a greater dose and more frequent delivery schedule than necessary to stop cancer cells before they start growing. Methods: In a mouse model, three different types of imaging will be used to accurately deliver the radiation, track individual cancer cells in the brain and assess the inflammation in the brain following irradiation. Results: The three types of imaging will provide information that will guide us to a novel preventative radiation dose and delivery schedule that has reduced side effects while maintaining its effectiveness. Discussion: The results of this research will be used to translate the imaging methods applied to measure inflammation from cancer treatments in patients.

A PET/MRI Reporter Gene Cell System for cell tracking

Shalaby, Nourhan, Kelly, John, Martinez, Francisco, Hicks, Justin Scholl, Timothy, Ronald, John

Cell-based immunotherapies have been in development for many decades but only recently have had remarkable successes, particularly in oncological applications. For an effective treatment response, it is important that these therapeutic cells are injected accurately, home to the correct locations, and persist long enough at these sites to illicit therapeutic functions. Biopsies and blood tests to assess the treatment responses of these therapies provide limited information based on circulating cells and other biomarkers. Thus, non-invasive in-vivo methods to track these cell therapeutics is needed. Multi-modal imaging is a technique that harnesses the benefits of more than one imaging tool to answer questions on cell viability, functionality, biodistribution and persistence of transplanted therapeutic cells. In this work, we are investigating the benefits of a dual PET and MRI reporter gene system that is safe, sensitive and allows for optimization of cell-tracking information from both modalities. We have successfully developed and validated a human-derived PET and MRI reporter gene system for cell tracking purposes. We confirmed that our engineered cells expressed both PET and MRI reporter genes and validated their ability to uptake their respective imaging tracers. This system combines quantifiable and sensitive information retrieved from PET with the feasibility and longitudinal tracking abilities of MRI by using human-derived genes with clinically approved imaging agents in a safe system that has high clinical translation potential for cell-tracking purposes.

Examining the regulation of the macropinocytosis of Amyloid Precursor Protein

J Krupa, C Seah, A Tsang, S Pasternak

Increasing evidence has supported a critical role for the lysosome, a cellular compartment responsible for the breakdown of material, in the cleavage of Amyloid Precursor Protein (APP) to Amyloid-β (Aβ). Prior work has demonstrated that macropinocytosis is involved in rapid and direct trafficking of cell-surface APP to lysosomes (Fig. 1). APP has long been suggested to function as a cell-surface receptor and its binding/crosslinking has been shown to increase its internalization to lysosomes and production of Aβ. Arf6 is a small GTPase known to be involved in the initiation of macropinocytosis and activation of downstream small GTPases such as Rac1, RhoA, and Cdc42. In the macropinocytosis of APP, an adaptor protein called Fe65 may serve as an initiator of this cascade as it binds to both APP and Arf6. We hypothesize that a signaling cascade is responsible for regulation of the macropinocytosis of APP. Specifically, we propose that the binding and crosslinking of APP recruits Fe65, which recruits and activates Arf6, which in turn activates Rac1, RhoA and Cdc42, resulting in the initiation of macropinocytosis (Fig. 2). To study this, a novel technique using Protein G beads to bind/crosslink APP at the plasma membrane has been developed (Fig. 3). This will allow for the precise observation of colocalization between bound/crosslinked APP and regulatory proteins. We predict that we will observe a specific spatial and temporal recruitment of these different regulatory proteins to bound/crosslinked APP. This observation could serve to identify new therapeutic targets to decrease Aβ load in Alzheimer's disease.

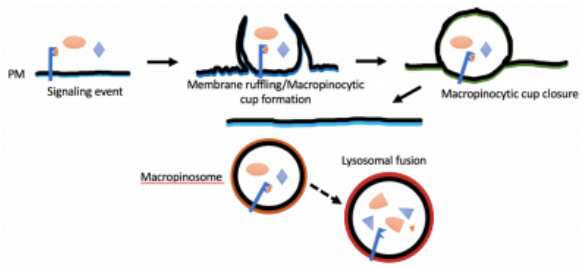

Figure 1. Diagram of the distinct stages of macropinocytosis

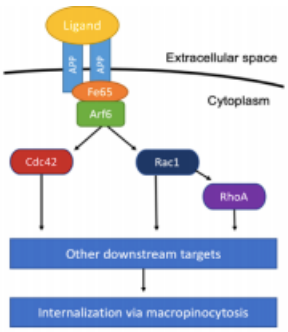

Figure 2. Proposed signalling cascade.

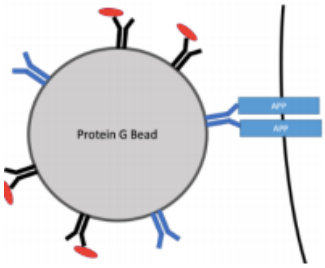

Figure 3: Novel Protein G bead conjugation technique. Protein G beads can be coated in an anti-APP antibody, as well as a fluorescently tagged secondary antibody. Cells expressing APP can be incubated with these beads to bind/crosslink APP at the plasma membrane. This will be used to observe the recruitment of our proposed signalling cascade to the membrane locations of bound APP.

Anti-metastatic role of Thrombin activatable fibrinolysis inhibitor (TAFI) and thrombomodulin in the breast cancer microenvironment.

Tasnim Reza, Zainab A. Bazzi, Michael B. Boffa

Thrombin activatable fibrinolysis inhibitor (TAFI) is a plasma zymogen that is activated (TAFIa) most efficiently by thrombin in complex with thrombomodulin (TM). TAFIa removes C-terminal lysine and arginine residues from cell-surface plasminogen receptors. The C-terminal lysine on cell-surface receptors is essential for binding plasminogen and its subsequent activation to plasmin. Plasmin can cleave many extracellular matrix (ECM) components and can activate proteases, which further degrade ECM, allowing invasion and metastasis of cancer cells. TAFIa can regulate pericellular plasmin formation, and higher TM expression has led to better prognosis in breast cancer. We propose that the promotion of TAFI with TAFI-specific TM will attenuate metastasis of breast cancer in vivo. MDA-MB-231 cells were transduced with lentivirus to express full-length TM that is wild-type (Wt TM) or TAFI specific (F376A/M388A TM) as well as tdTomato and firefly luciferase from a tricistronic expression system. The control cells express tdTomato and firefly luciferase but do not express TM. The Wt TM-expressing cells activated both TAFI and Protein C (PC), and the F376A/M388A TM-expressing cells activated TAFI but do not activate PC, whereas the control cells activated both TAFI and PC due to endogenous expression of TM by the cells. NOD SCID gamma (NSG) mice were injected with TM expressing cells. Following the injection, the primary tumour continuously grew in all cases, with apparently greater growth for the control cells. The metastasis was primarily observed in the axillary lymph node of some control and Wt TM mice but not in mice implanted with cells expressing TAFI-specific TM.

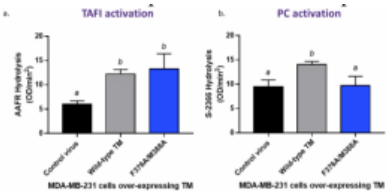

Figure 1: Activation of TAFI (a.) and PC (b.) by cells expressing wild type TM (no mutation), and cells expressing F376A/M388A mutant TM. Different letters refer to conditions that are significantly different from each other ($p < 0.05$) by one-way ANOVA with Tukey post-hoc analysis (n=3).

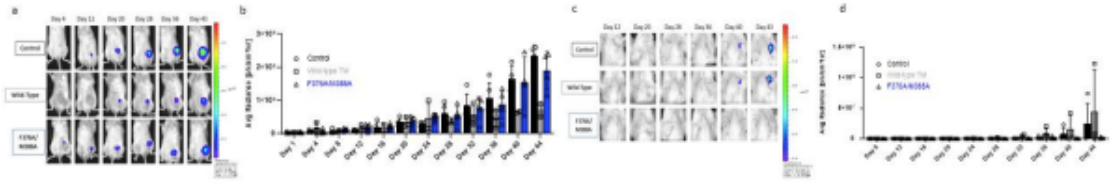

Figure 2: (a.) The growth of the primary tumour represented by the growth of the BLI signal in the mammary fat pad for 43 days. (b) The quantification of the signal observed in the BLI. The mice represented are injected with Control (no TM), WT, and F376A/M388A TM-expressing cells (n= 3 – 4). (c.) Metastasis of cells to the lymph nodes observed in mice injected with Control (no TM), WT, and F376A/M388A TM-expressing cells. (d.) The quantification of the signal observed in the axillary lymph nodes of mice. (n= 3 – 4).

Direct Evidence for the Intracellular Non-Covalent Interaction of Apolipoprotein(a) and ApolipoproteinB100 during Lipoprotein(a) Biosynthesis

Amer Youssef, Michael B Boffa, Santica Marcovina and Marlys L Koschinsky

Elevated plasma lipoprotein(a) [Lp(a)] levels, present in > 20% of the global population are associated with increased risk for atherosclerotic cardiovascular and calcific aortic valve diseases. As such, novel approaches to Lp(a) lowering including inhibition of particle formation are promising avenues for drug discovery. However, Lp(a) biosynthesis remains poorly understood, with the locations of the non-covalent and covalent steps of Lp(a) assembly unclear. In the current study, we set out to locate the non-covalent interactions. We used HepG2 cells transiently expressing 17 kringle (17K) r-apo(a), or a 17KΔLBS7,8 variant with mutated weak lysine binding sites that impairs its non-covalently binding to apoB. Cell lysates and media were co-immunoprecipitated using apo(a)- and apoB-specific antibodies. We found that non-covalent complexes containing apo(a)/apoB are only present in 17K and not 17KΔLBS7,8 apo(a) lysates, while covalent apo(a)/apoB complexes were significantly diminished in 17KΔLBS7,8 media. By confocal microscopy, 17K apo(a) and apoB colocalized intracellularly and consistently overlapped with staining for the ER marker calnexin, the trans-Golgi marker TGN46 and the early endosome marker EEA1, and less so with the lysosomal marker LAMP1. The 17KΔLBS7,8 apo(a) had lower colocalization with apoB, and less overlap with calnexin and TGN46. Most importantly, using a proximity ligation assay, we directly documented interactions between 17K apo(a) and apoB intracellularly, interactions that were dramatically reduced for 17KΔLBS7,8. In conclusion, apo(a) and apoB interact non-covalently within the secretory pathway of HepG2 cells. These findings explain the ability of agents that inhibit apoB biosynthesis, such as mipomersen and lomitapide, lower Lp(a) levels.

Microstructural characterization and Visualization a 3D printed phantom using diffusion MRI and microscopy

Farah N. Mushtaha, Tristan K. Kuehn, Omar El-Deeb, Amanda Moehring, Ali R. Khan, Corey A. Baron

Introduction. Diffusion MRI (dMRI) is promising to quantify a brain's histological features at micrometer scales. However, there is no "ground truth" to validate it. We investigate a novel phantom produced using fused deposition modeling 3D printing with a dual-component material hat consists of an elastomer and poly vinyl alcohol (PVA) (PORO-LAY 2) that dissolves in water, leaving behind microspores that can mimic diffusion characteristics of axons (Fig.1). Here, we characterize Diffusion Kurtosis Imaging (DKI) parameters in dMRI phantoms, assess their reproducibility, and visualize their microstructure. Methods. Four identical phantoms were created by printing 11mm radius cylinders with 100µm thick layers of parallel lines to mimic linear fibers. The phantoms were immersed in water for 168hrs and stacked in a test tube with water for imaging. dMRI was implemented in a 9.4T scanner. DiPy 3 was used to compute DKI-derived metrics. To visualize the microspores, a phantom block was prepared using the outlined procedure then sliced into 50µm slices. RhodamineB was used to stain the elastomer component. Confocal microscopy was performed using a Leica SP5 laser system and a 40X dry objective lens. Results. Coefficients of variation across different phantoms of identical parameters were less than 15% in DKI-Parameters (Table.1). Confocal microscopy images revealed larger pores on the order of 70µm caused by the printing pattern and smaller pores on the order of 2- 30µm caused by PVA dissolving (Fig.2). Conclusion. 3D printed phantoms possess 2µm wide pores that could mimic axons in white matter, serving as complex, anatomically accurate phantoms.

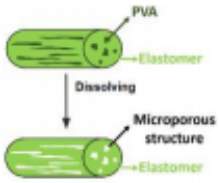

Figure 1. Illustration of PORO-LAY before and after immersing it in water.

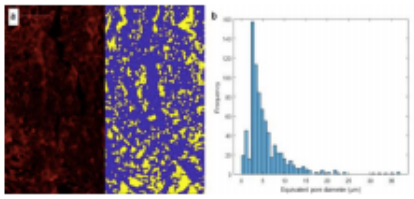

Figure 2. a) Fluorescent microscopy image before (left) and after (right) performing pore segmentation. b) Histogram of equivalent diameter of pores obtained from segmentation and their frequency

Table 1. Mean dMRI values from a nominal phantoms and the coefficient of variation. Note: (axial kurtosis, AD; radial kurtosis, RD; Mean kurtosis, MK; axial diffusivity, AD; radial diffusivity, RD; Mean diffusivity, MD; fractional anisotropy, FA)

Metric	Mean Value	Coefficient of variation (%)
AD (mm^2/s)	0.00213	3.19
RD (mm^2/s)	0.00101	13.20
MD (mm^2/s)	0.00138	8.78
FA	0.4622	5.24
AK	0.0734	10.10
RK	1.1333	6.31
MK	0.5247	1.86

Multi-view 3D echocardiography volume compounding for mitral valve procedure planning

Patrick Carnahan, John Moore, Daniel Bainbridge, Elvis C.S. Chen, and Terry M. Peters

Echocardiography is widely used for obtaining images of the heart for both preoperative diagnostic and intraoperative purposes. For procedures targeting the mitral valve, transesophageal echocardiography (TEE) is the primary imaging modality used as it provides clear 3D images of the valve and surrounding tissues. However, TEE suffers from image artifacts and signal dropout, particularly for structures lying below the valve including chordae tendineae. In order to see these structures, alternative echo views are required. However due to the limited field of view obtainable,the entire ventricle cannot be directly visualized in sufficient detail from a single image acquisition in 3D. This results in a large learning curve for interpreting these images as the multiple views must be reconciled mentally by a clinician. We propose applying an image compounding technique to TEE images acquired from single mid-esophageal position and multiple transgastric positions in order to reconstruct a high-detail image of the mitral valve and sub-valvular structures. This compounding technique utilizes a semi-simultaneous group-wise registration to align the multiple 3D volumes, followed by a weighted intensity compounding step. This compounding technique is validated using images acquired of a custom silicone phantom, excised porcine mitral valve units, and two patient data sets. We demonstrate that this compounding technique accurately captures the physical structures present, including the mitral valve, chordae tendineae and papillary muscles.

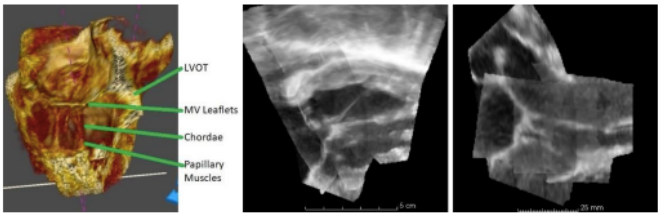

Figure 1: Visualizations of compounded TEE data from five different TEE volumes. Left, a volume rendering view. Middle, a commissure-commissure view. Right, an AP view.

Ultrasound-Based Microvascular Parameters for Classification of Anti-Angiogenic Tumor Treatment Response: A Scalable Preclinical Approach

Mahsa Bataghva, Danielle Johnston, Nicholas Power, Silvia Penuela, James C. Lacefield

Initial steps towards a scalable preclinical platform for anti-angiogenic treatment response classification in cancer models based on multiparametric microvascular ultrasound is presented. The foundations of the platform are a rapid tumor angiogenesis assay using an ex-ovo chicken embryo chorioallantoic membrane (CAM) model, and classification algorithm. A computational model using multi-parametric perfusion properties computed from three-dimensional power Doppler and 2D contrast-enhance ultrasound images of tumor blood flow, Caki-1 kidney tumor cells engrafted in the CAM of chick embryo, is proposed and repeatable quantitative perfusion features are identified to be used in machine-learning model. More specifically, Vascular index (VI) and tumor volume estimated from PD with an IIR clutter filter and the area under the wash-in curve (AUC), representing intra-tumor microvessel density estimated from nonlinear CEUS images were computed. A dataset of 37 tumors, where 19 CAMs were sunitinib treated and the remainder were controls, was constructed with three above-mentioned features. A logistic regression learning algorithm was used to classify control and treated groups. The classifier with VI + AUC features achieved accuracy, sensitivity, and specificity of 89%, 95%, and 80%, respectively based on 10-fold cross-validation. The classifier including all 3 features achieved accuracy, sensitivity, and specificity of 88%, 95%, and 75%, respectively. Furthermore, the VI + AUC classifier also outperformed two-feature classification based on VI and volume or AUC and volume, indicating that 3-D PD and 2-D CEUS provide complementary information about tumor perfusion in the CAM assay. Therefore, we are optimistic this assay will also be useful for evaluating combinations of established and novel perfusion features.

Comparing detection limits of Magnetic Particle Imaging (MPI) to Magnetic Resonance Imaging (MRI) using super paramagnetic iron oxide nanoparticles in a breast cancer metastasis model

Kierstin P Melo, Ashley V Makela, Amanda M Hamilton1, and Paula J Foster

Introduction: Magnetic particle imaging (MPI) is a new imaging modality that sensitively and specifically detects superparamagnetic iron oxide nanoparticles (SPIONs) within a sample. Our lab has shown that SPION-based MRI cell tracking has very high sensitivity, but low specificity. MPI cell tracking could overcome these challenges. Methods: MDM-AB-231BR cells labeled with MPIO, mice were intracardially injected with either 2.5 x 105 or 5.0 x 105 cells. MRI was performed in vivo the same day at 3T using a bSSFP sequence. After mice were imaged ex vivo with MPI. In a second experiment, mice were injected with 5 x 10 4 4T1BR cells, labelled with either MPIO or the SPION Vivotrax. MRI and MPI was performed in vivo. Results: Signal from MPI and signal voids from MRI both showed more iron content in mice receiving an injection of 5.0 x 105 cells than the 2.5 x 105 injection. In the second experiment, in vivo MRI was able to detect signal voids in the brains of mice injected with Vivotrax and MPIO, although voids were fainter in Vivotrax labeled cells. In vivo MPI signal was only detectable in mice injected with MPIO-labeled cells. Conclusion: This is the first example of the use of MPIO for cell tracking with MPI. With an intracardiac cell injection, approximately 15% of the injected cells are expected to arrest in the brain vasculature. For our lowest cell injection of 5.0 x 104 cells this is ~7500 cells.

MiRNA expression in motor neurons of the oculomotor nucleus in ALS

McLellan, C., Campos-Melo, D., Martin, A., Hammond, and Strong, M.

Individuals living with amyotrophic lateral sclerosis (ALS) experience voluntary muscledegeneration caused by death of upper and lower motor neurons. Almost all ALS patients retain eye motor function indicating that motor neurons of the oculomotor nucleus are resistant to ALS-associated death. Alterations in RNA metabolism have been described in ALS spinal cord including a downregulation of numerous miRNAs – small non-coding RNA molecules that control gene expression. We hypothesize that specific miRNAs involved in neuroprotection are upregulated in ALS oculomotor nucleus. Fluorescent in situ hybridization (FISH) was used to detect miRNA expression in fixed tissue of midbrain (oculomotor nucleus), medulla (hypoglossal nucleus) and spinal cord of ALS and control patients. FISH was performed with DIG-labeled probes to miR-9-5p, miR-182-5p, and miR-124-3p. Sections were imaged with a Leica SP8 confocal microscope and motor neurons were quantified for fluorescence intensity using Fiji-ImageJ. miR-9-5p, miR-182-5p, and miR-124-3p were upregulated in ALS oculomotor nucleus compared to control oculomotor nucleus. These miRNAs were upregulated to a lesser extent in ALS hypoglossal nucleus for miR-182-5p and miR-124-3p. miR-182-5p and miR-9-5p showed no change in expression between ALS and control spinal cord, whereas miR-124-3p was downregulated in ALS spinal cord. These preliminary results indicate that several miRNA species are upregulated in ALS oculomotor nucleus. Future work will elucidate the role of miRNAs in oculomotor function in ALS. Understanding molecular and pathological differences between the oculomotor nucleus and spinal cord may reveal pathways that permit resistance to ALS progression and new targets for disease treatment.

Characterization of an N-terminal tau cleavage fragment associated with the phosphorylation of tau at Thr175

N. Donison, K. Volkening, M. A. Hintermayer & M. J. Strong

Chronic traumatic encephalopathy (CTE) is a neurodegenerative disease characterized by the presence of cytoplasmic microtubule-associated protein tau (tau) aggregates and fibrils. Tau protein is subject to various post-translational modifications including phosphorylation and truncation, which contribute to tau's propensity to form pathological aggregates. Previous research has demonstrated that in a rodent model of traumatic brain injury (TBI), CTE-like pathology was initiated and characterized by the phosphorylation tau at Thr175 and Thr231 acutely following the injury. Phosphorylation of tau at Thr175 results in a conformational change leading to the exposure of the N-terminal phosphatase activating domain (PAD). Exposed N-terminal PAD is able to initiate a molecular cascade resulting in the phosphorylation of tau at Thr231 and the formation of pathological fibrils. Here we examine the production of an N-terminal PAD+ tau cleavage fragment in the presence of pThr175 tau in vitro and in vivo. First, transfection of pseudo-phosphorylated Thr175 tau in Neuro2A cells produces a PAD+ fragment. Secondly, analysis of brain lysates from a rodent model of TBI results in the presence of PAD+ fragment in TBI rodents only, compared to non-injured controls. Regression analysis of both the in vitro and in vivo immunoblots suggest that the PAD+ fragments are of similar size and thus of similar origin. Future experiments will determine the protein sequence of the fragments by mass spectrometry. Once the fragments have been sequenced, they will be cloned and transfected into Neuro2A cells to determine the bioactive nature and pathologic capabilities, including tau phosphorylation and fibril formation.

Robust Retrospective Eddy Current Correction for Diffusion MRI

Jake Valsamis, Dr. Corey Baron

Introduction: Diffusion MRI (dMRI) is a powerful diagnostic tool whose potential is burdened by artefacts. Eddy currents (ECs) induced by dMRI gradients corrupt data integrity, leading to distortions and blurring in dMRI images. The current gold standard for EC correction, FSL eddy, assumes that ECs don't decay with time. However, some advanced forms of dMRI, such as oscillating gradient dMRI, induce large ECs that decay over time. In this case, FSL's simplifying assumptions do not accurately reflect the experimental conditions, and considerable artefacts remain. To overcome FSL's limitations, we have developed a novel approach to characterize EC behavior using the acquired data. Methods: Diffusion MRI data was acquired in a single scan using both pulsed and oscillating gradients. Opposite polarity diffusion gradients were used to induce distortions along opposite directions. Our method consists of a novel optimization technique that finds the EC parameters that minimize the difference between images with inverse distortions. Results: For the eight pairs of images with inverse distortions acquired, on average, correction with our method results in 12% higher image similarity than correction with FSL eddy (FIG1). For volumes acquired with oscillating gradients, qualitative assessment shows our method's ability to correct blurring not corrected by FSL eddy. Discussion: Our method's ability to account for the decaying behaviour of ECs allows improved correction over FSL eddy. A robust algorithm capable of correcting EC distortions will ensure dMRI diagnoses are not limited by the effects of the hardware inherent to its function.

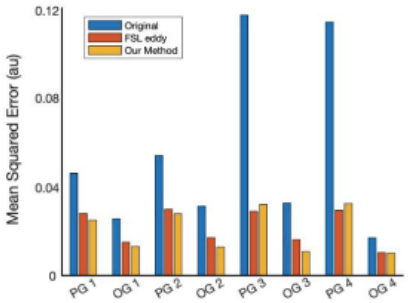

Figure 1: Quantitative assessment of similarity between pairs of images with inverse distortions prior to correction, after correction with FSL eddy, and after correction with our method. PG and OG indicate volume pairs acquired with pulsed gradients and oscillating gradients, respectively.

Dopaminergic modulation of a fast visuomotor pathway in Parkinson's disease

M. Gilchrist, R. Kozak, M. Prenger, B. Corneil, P.A. MacDonald

Parkinson's disease (PD) is a neurodegenerative disease associated with loss of dopaminergic input to the basal ganglia (BG). This significantly impairs voluntary movement, however much less is known about the effect of PD on the fast visuomotor pathway. This study aims to elucidate the role of the BG in the contextual control of fast visuomotor responses by studying stimulus-locked responses (SLRs) in PD patients. The SLR is the rapid recruitment of limb muscles within 100ms of visual stimulus onset which drives the arm towards the stimulus. 20 PD patients and 20 healthy controls (HC) will perform a reaching task using a Kinarm robot. They will reach either towards (pro-reach) or away from (anti-reach) a moving target on a screen, depending on the instruction given by the colour of the fixation point before the target emerges. The instruction time will be either 500 or 1000ms. Surface electrodes will record muscle activity during the task. Participants will perform one session on, and one session off dopamine (DA) medication. Contextual control of visuomotor responses will be assessed by comparing SLR magnitude on pro- vs anti-reach trials. I hypothesize that contextual control of the fast visuomotor pathway is compromised by PD, and that DA medication will mitigate this deficit. I predict PD patients will produce SLRs of equal magnitude during pro- and anti-reach trials off DA, but larger SLRs on pro-reach trials on DA. This study will clarify the role of dopaminergic input to the BG in control of the fast visuomotor pathway.

Design and 3D Printing of Wireless Load Cells for Biomedical Applications

William D Anderson, Sydney Wilson, David W Holdsworth

Introduction: Load data provides quantitative information about the forces acting on structures. Advancements in automotive pressure sensor technology have enabled an alternative method of monitoring real-time load data. To be effective, the sensor package must be embedded within a deformable enclosure designed to transduce compression. Objective: The objective of this study is to develop customizable, 3D printed load cells capable of measuring a range of compressive loads for use in biomedical applications. Materials and Methods: Generating a two-component rectangular structure with four internal cantilever beams produced a deformable compression enclosure. In subsequent designs, the width of the beams was increased from 2 mm to 4 mm. The enclosure was imported into Abaqus to determine the theoretical load capacity when fabricated in polylactic acid (PLA) and Ti-6Al-4V (Figure 1a). To determine the experimental load capacity of the enclosures, the packages were 3D printed in PLA and subjected to compressive deformation applied by an Instron. Results: The theoretical and experimental load capacity of the PLA enclosure ranged from 5 to 12 N (Figure 1b). The average percent error between the theoretical and experimental PLA load capacity was 2.62%. The theoretical load capacity of the Ti-6Al-4V enclosure ranged from 210 to 460N. Discussion and Conclusions: In combination with our load sensor, a retasked tire pressure sensor, we will be able to develop a range of wireless telemetric load cells with varying load capacity. The device could be used to measure orthopaedic loads within joint replacements, fracture fixation components, and spinal fusion cages.

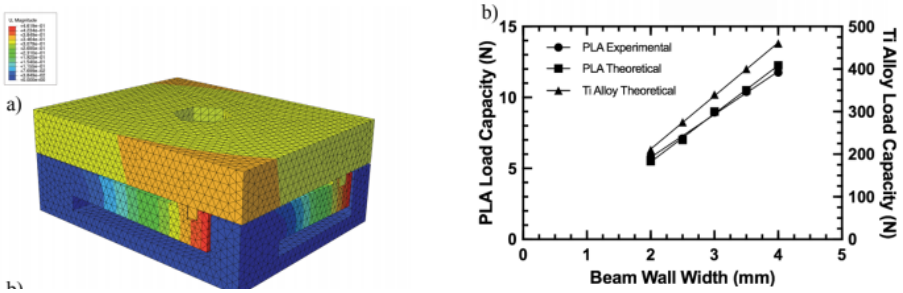

Figure 1: (a) FEA of two-component compression enclosure. (b) Results of FEA and compression testing, PLA/Ti Alloy load capacity vs. beam wall width